DEGREE PROJECT IN ELECTRICAL ENGINEERING,
SECOND CYCLE, 30 CREDITS
STOCKHOLM, SWEDEN 2017

MPC Design For Autonomous Drifting

CORVIN KÜCK

KTH ROYAL INSTITUTE OF TECHNOLOGY
SCHOOL OF ARCHITECTURE AND THE BUILT ENVIRONMENT

Sammanfattning

Målet med denna studie är att undersöka prestandan för olika reglerstrukturer när en radiostyrd bil driftar. En cykelmodell och en empirisk däcksmodell används för att modellera bilen. Parametrarna som användes för Fiala däcksmodellen är framtagna genom experiment och simuleringsresultatet av den modellerade bilen jämförs med verklig data. En stabilitetsanalys är också gjord för det modellerade systemet. Systemet är sedan linjäriserat runt ett jämviktsläge för drifting för att kunna skapa en regulator. En tillståndsregulator med återkoppling används för att stabilisera systemet. Förstärkningskonstanterna för regulatorn optimeras med linjärkvadratisk reglering och sedan designas en modell prediktiv kontroller. Slutligen utvärderas prestandan, genom simulering, hos de tre regulatorerna när en störning finns i systemet.

Abstract

The goal of this thesis is to evaluate the performance of different controllers to keep a remote-controlled vehicle in a sustained drift. A bicycle model and an empirical tyre model are used for modelling the vehicle. The parameters for the used Fiala tyre model are experimentally identified and the simulation results of the modelled vehicle are compared to measured experimental data. It follows a stability analysis of the modelled system. The system is then linearized around one of the drift equilibria to allow controller design. A state feedback controller is designed to stabilize the system, the controller gains are optimized using a Linear Quadratic Regulator (LQR) design, subsequently a Model Predictive Controller (MPC) is designed. Finally, the performance of the 3 controllers is evaluated for a simulation with a disturbance acting on the system.

TABLE OF CONTENTS

1 INTRODUCTION

The traffic in the world and the number of cars is rapidly increasing. In 2010, the number of registered cars in the world first hit the 1 Billion mark and continuous growing [1]. The increasing traffic imposes challenges for the environment and on human safety. Autonomous cars can help to reduce these problems, as they can achieve a better road flow and reduce the risk of accidents among other benefits. However, there are still many obstacles that have to be dealt with in order to introduce fully autonomous cars for a wider use. The technical issues are just one part, other obstacles are the question of liability and public acceptance. For public acceptance, it is important to make the cars as safe as possible and to be able to control them in extreme manoeuvres. One of these extreme manoeuvres is the drift, where only skilled drivers manage to control a car. Therefore, this thesis focuses on controlling a car during drifting. The goal of the thesis is to analyse the stability of a remote-controlled vehicle and find an appropriate drift equilibrium for a sustained drift manoeuvre, where the slip angle and the yaw rate stay constant. Another goal of the thesis is to increase the performance of previous control approaches by using Linear Quadratic Regulator (LQR) design and Model Predictive Control (MPC).

The section 1.1 introduces autonomous driving, where benefits, drawbacks and obstacles will be described. Furthermore, an introduction to the history and the state of the art of autonomous driving will be given.

Section 1.2 describes what drifting is and explains what benefits are to be expected from controlling the drift. Moreover, previous work in this field is introduced. Additionally, it describes the modelling of tyres.

The Sections 1.3 and 1.4 present the design and background of the LQR and MPC controller, respectively.

In Section 1.5, the remote-controlled vehicle and the experimental setup are described.

The modelling of the vehicle including the experiments for the empirical tyre model and experiments to verify the model is presented in section 2.

Section 3 displays the equilibria of the system for different steering angles and examines the behaviour of the system around these equilibria using phase portraits.

The linearization of the system and the design of a state feedback (SF) controller is presented in section 4. It also contains the tuning of the SF gains using LQR design and the design of a MPC.

The performance of the different controllers is evaluated using a simulation with a disturbance acting on the friction of the front tyre. The results are shown in section 5.

Finally, section 6 discusses the results, draws conclusions and illustrates possibilities to pursue the work in this thesis.

1.1 Autonomous driving

The most common frame to describe the level of automation of a vehicle is the one released by the National Highway Traffic Safety Association (NHTSA) [2]. It describes the automation in 5 steps.

- No-Automation (Level 0): The driver is in complete and sole control of the primary vehicle controls – brake, steering, throttle, and motive power – at all times.
- Function-specific Automation (Level 1): Automation at this level involves one or more specific control functions. Examples include electronic stability control or pre-charged brakes, where the vehicle automatically assists with braking to enable the driver to regain control of the vehicle or stop faster than possible by acting alone.
- Combined Function Automation (Level 2): This level involves automation of at least two primary control functions designed to work in unison to relieve the driver of control of those functions. An example of combined functions enabling a Level 2 system is adaptive cruise control in combination with lane centring.
- Limited Self-Driving Automation (Level 3): Vehicles at this level of automation enable the driver to cede full control of all safety-critical functions under certain traffic or environmental conditions and in those conditions to rely heavily on the vehicle to monitor for changes in those conditions requiring transition back to driver control. The driver is expected to be available for occasional control, but with sufficiently comfortable transition time. The Google car is an example of limited self-driving automation.
- Full Self-Driving Automation (Level 4): The vehicle is designed to perform all safety-critical driving functions and monitor roadway conditions for an entire trip. Such a design anticipates that the driver will provide destination or navigation input, but is not expected to be available for control at any time during the trip. This includes both occupied and unoccupied vehicles.

1.1.1 Benefits, drawbacks and obstacles of autonomous driving

In the US, about a third of CO2 emissions are caused by transportation, where traffic conduction plays a significant role [3]. Autonomous cars are expected to produce a better traffic flow and to be more efficient, this gives a high potential to reduce fuel consumption and emissions caused by traffic [4].

In 2015, the number ten of leading causes of death in the world was road traffic injuries, for 2030 the World Health Organization (WHO) predicts it to be number five [5] [6]. Where a study of the NHTSA came to the conclusion, that 94% of accidents were caused by human failure [7]. The number of accidents and with it all the caused grief and financial effects could be greatly reduced by autonomous vehicles [4].

Besides these points, autonomous cars also offer the chance of increased mobility for the young, elder and handicapped people [8]. They also give new possibilities to car-sharing, reduce the need for double-traveling and reduce the area needed for parking. It would also make traveling by car more convenient, since the passengers could use the time for other tasks.

However, there are also negative effects expected when introducing autonomous driving on a larger scale. The high convenience might lead to more traveling. Many jobs directly (e.g., public transit) and indirectly (e.g., crash repair) related to driving will be affected [4]. Liability questions might become harder to answer.

There is also a risk of cyber-attacks and privacy concerns are getting stronger as more and more data is obtained by sensors and by some manufacturers saved and used for research purposes [9] [10]. These privacy concerns are getting even stronger when data is sent to other cars (Vehicle to Vehicle (V2V)) or to the Infrastructure (Vehicle to infrastructure (V2I)) for coordination and optimization [11] [12].

Technology is already very close to making the dream of fully autonomous driving come true, but there are still some aspects that need improvement. While the sensing of cars using different types of sensors like LIDAR and cameras often exceed the possibilities of humans, the interpretation of this data can still be improved.

Another obstacle for the introduction of autonomous cars is the willingness of the passengers to give away their control over the car. However, some Advanced Driving Assistance Systems (ADAS) already take control over the car for specific scenarios, such as parking and are accepted by many drivers. The public acceptance of autonomous cars largely depends on their safety and how they should behave during unpreventable accidents. Even though many studies show, that autonomous cars will be safer than traditional cars, many people still lack trust in these systems [4] [13] [14] [15]. Building trust in autonomous vehicles can be done by introducing ADAS, such as adaptive cruise control, that offer some extend of autonomous driving. Further increasing the performance and safety of autonomous vehicles is also crucial. Furthermore, there must be public discussions about how cars should behave in unpreventable accidents (e.g., the famous trolley-problem) and laws must be made to regulate how the machines should decide in different scenarios [16] [17].

1.1.2 History of autonomous cars

Self-driving autonomous cars have been a dream for a long time, and first attempts to make this dream a reality have been made as early as 1925, with a radio operated car [18]. Most works on self-driving cars at that time were based on guiding circuits in the roads [19] [20] [21].

A big step forward was the Prometheus project, carried out 1987-1995. In the first step, they managed to track other vehicles, drive in lanes and change lanes autonomously to pass other cars. During these tests, more than a thousand kilometres were travelled with speeds up to 130 km/h. In 1995, another car travelled more than 1300 km with speeds up to 180 km/h, also performing lane changes to pass other cars autonomously. The longest distance travelled without driver interaction was 158 km, the driver had to interact every 9 km on average [22].

In the same year, there was another test carried out in the USA where even more than 98% of the distance was traveled without human interaction to the steering. However, for safety reasons, the throttle and the brakes were controlled by a driver [23].

More recently, competitions in the field of autonomous driving have been carried out by the Defense Advanced Research Projects Agency (DARPA). The first DARPA Grand challenge has been carried out in 2004, where the cars had to travel 240km through the Mojave Desert. In this competition, the furthest a car managed to travel was less than 20 km. However, in the following year, the competitors were much more successful, five teams completed the whole track, including several obstacles, such as narrow tunnels and sharp turns. Since then, several competitions have been carried out by DARPA, which also get a high recognition by the public [24].

During the last decade tests on public streets were carried out by several car manufacturers and research facilities, with increasing level of automatization and less human interventions [25] [26] [27] [28] [29]. In 2013, researchers from the KIT, Germany sent a Mercedes-Benz S-class on a 100 km test-drive, over highways, country-roads and through towns. The car completed the course fully autonomously. It also managed to follow the traffic regulations at traffic lights, road crossings and even with oncoming traffic in narrow streets. Furthermore, it is interesting, that the used sensors were close to the sensors included in the regular production car [30].

1.1.3 State of the art

Most cars nowadays exhibit some kind of Advanced Driver Assistance System (ADAS), that correspond to level 1 or level 2 on the NHTSA scale. Examples of this are the anti-lock braking system and Electronic Stability Control (ESC). More recently parking assistance systems, cruise control, active lane keeping assistance and collision avoidance systems were developed and implemented. These systems were shown to increase the safety and gained a high acceptance by the customers.

BMW, Ford, Volvo and Tesla announced that they want to launch tests on public roads with level 3 automatization in 2017 [31] [32] [33].

1.2 Drifting

In many works related to drifting, a bicycle model similar to Figure 1 is used. In this model, both wheels on each axis are lumped together, lateral dynamics, such as roll and weight transfer, are neglected. The distances between the Centre of gravity (COG) and the front and the rear axle are a and b respectively. The yaw rate is the planar rotation around the z-axis and is referred to as r. F_{yf} and F_{yr} are the lateral forces on the front and rear wheels, respectively. The steering angle δ is the input. The tyre slip-angles are α_f and α_r. The velocity vector V, consists of the longitudinal velocity v_x and the lateral velocity v_y. The high sideslip angle β is descriptive for the drift and it is defined as

$$\beta = \arctan\frac{v_y}{v_x}.$$

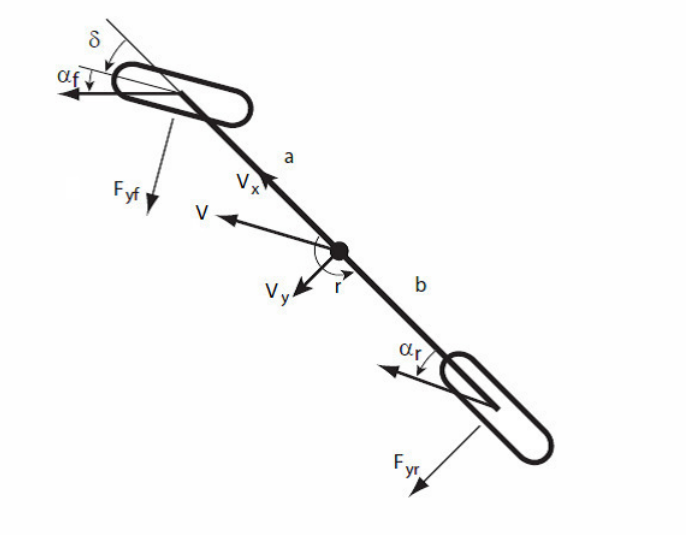

Figure 1: Bicycle model [34].

Another important concept for drifting is the friction circle. The forces that can be transferred by the tyres are limited by the friction between the tyres and the ground. The maximum force is also influenced by the downforce, which can vary because of aerodynamic effects and weight transfer. For simplicity, we assume an isotropic tyre, where the maximum forces in longitudinal and lateral direction are equal.

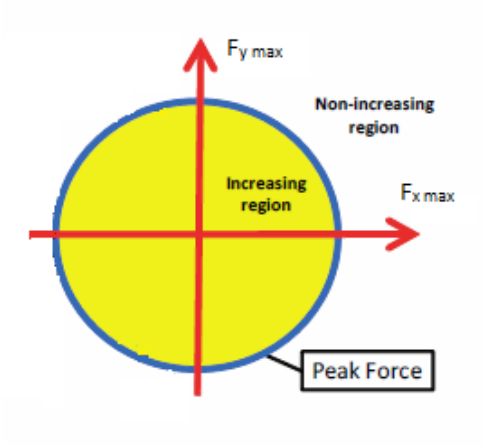

Figure 2: Friction-circle [34].

The maximum force a tyre can transfer is shown as the outside of the circle (blue circle). It can be purely in x or y direction or a combination of these. During usual driving, the tyre forces are not saturated and the combined tyre forces are well inside the friction circle (yellow area). This means that there are reserves of tyre force in both directions to control the car. Professional race drivers try to use the maximum tyre force corresponding to the outside of the circle (blue circle). If they apply $F_{y\,max}$ as a braking force, the tyre force is saturated and no force in x-direction can be applied. To regain the possibility to steer the car, the race car driver has to reduce the brake input. Similar behaviour is apparent during the drift, where a high throttle input is used and the longitudinal tyre force is close to $F_{y\,max}$. In this stage, just very little lateral force can be transmitted by the tyre, which allows the car to spin out and move sideways [35].

1.2.1 What is drifting

Cornering while moving noticeably sideways is referred to as “drifting”. In this state, the rear-tyres are saturated and have a high longitudinal slip, this causes the characteristic high amounts of tyre smoke. Most drivers are not able to control the car during drifting, whereas professional race drivers are able to control the car and use their skills in drifting competitions or in rally races. They use abrupt throttle or break inputs to saturate the rear tyre force to initiate the drift. In the drift, they are able to keep the sideslip angle constant and follow a desired path by using counter steer and throttle input.

Drifting is mainly used in rally and dirt track races, where the friction coefficient between the tyres is low or varies a lot, like on snow or gravel. Under these circumstances cornering can be done faster when drifting is used [36].

1.2.2 Benefits of controlling the drift

It is more likely that the driver loses control over his car when the friction between the tyres and the ground is low or it changes suddenly. This can lead to potentially dangerous situations. Usually, the ADAS, such as ESC, attempt to prevent the vehicle to enter the drift. However, entering in the drifting situation could enable the car to make use of some positive effects that are apparent during the drift. The equilibrium sideslip angle in the drift is insensitive to the longitudinal velocity as well as to friction variations. Thus, drifting around a corner can be a safer, easier and more predictable way of cornering under unpredictable surface conditions [37]. Furthermore, a corner can be taken on a different trajectory when using drifting. Being able to control drifting would give a wider range of possibilities to handle the car in emergency situations and can help to increase the safety of the passengers and other traffic participants.

1.2.3 Previous work

In the last years, there have been several studies on drifting and controlling vehicles at the limits of handling. Some investigated how professional drivers control cars in the drift [35] [38] [37]. Another approach of gaining insight in the nature of drifting is analysing the steady-state drift equilibria. Several studies have shown that steady-state drifting corresponds to unstable equilibrium points. For example, in [37], for a bicycle model and in [39], for a more sophisticated 4-wheel model with weight transfer. The results of these investigations have been used to design controllers to govern vehicles at the limits of handling.

Throughout the studies a variety of different models and approaches have been used. In [40], and [41] the four-wheel model was used throughout the paper. In [42], the four-wheel model was used for the trajectory generation part and a bicycle model for the controller design. Bicycle models with 3-states or 2-states showed to achieve good results in [37], [43], [35], [44], [45], and [46].

The Fiala tyre force model was used in [42], [37], and [46]. In [35], a linear tyre assumption is used. The steering feedback is used to make up for the modelling errors caused by this assumption. Experimental evaluation showed the effectiveness of their approach. Another tactic is using Fuzzy-logic to identify steady-state and transient conditions as in [45]. When the transient case is identified, the kinematic formula is used to update the cornering stiffnesses of the bicycle model, otherwise a state-observer is used.

The friction circle has been used in [42], [37], and [35] to generate the throttle inputs while controlling the tyre slip. Controlling the front tyre slip can be used to ensure that enough lateral tyre force is available for steering. By controlling the rear tyre slip, e.g., the yaw-rate can be influenced.

As described in [42], usually the dynamics around the drift equilibria are linearized and stabilized by a controller. Additionally, a reference state is added to track a reference trajectory. This creates two problems. First, the problem becomes underactuated because of the additional state. Second, with the saturated rear tyres, a change in the throttle input influences the longitudinal force of the tyre, but also the lateral-force. This creates a coupling between the longitudinal and the lateral dynamics. To deal with this, [40] treats the rear lateral force as disturbance input. In the paper, a four-wheel model is used, where all tyres can be actuated separately. These inputs are used to deal with the disturbances.

In [42], the sideslip and the path are considered as directly related and the trajectory is treated as a sequence of drift-equilibria. These equilibria were evaluated with a four-wheel model. For the controller development, a simple bicycle model is used with the 3 states, namely, yaw rate, sideslip-angle and longitudinal velocity. The rear longitudinal force and the steering angle are used as inputs. From the lookahead error regulation and the sideslip stabilization they derive the control law on the lateral front- and rear tyre force. To map the lateral front tyre force to the steering angle they use the Fiala brush tyre model. The friction circle relation is used to map the lateral rear tyre force to a throttle command. The performance was tested with a car on dry-asphalt. The reference path and the sideslip angle were tracked with good performance with sideslip angles up to 45 deg.

In [42], a bicycle model with the lateral velocity and the yaw rate as states is employed, the only input is the steering angle. A Fiala tyre force model is used, a quasi-steady-state-ramp-steer manoeuvre is performed to obtain the cornering stiffnesses and the friction coefficient for the front and rear tyres. It follows an extensive investigation of the drift equilibria. They show that for small steering angles, the system inhibits three equilibria. For higher steering angles, the system only has one equilibrium, where high sideslip angles and counter steer angles are present, this corresponds to drifting. Analysis of the equilibrium shows the mentioned insensitivity of the equilibrium sideslip angle to variations in the longitudinal velocity and friction coefficients. However, it is also shown that the yaw rate shows significant variations with changing longitudinal velocity and friction coefficient.

Additionally, to the sensitivity analysis, a phase portrait analysis is done to gain insight of the system behaviour around the equilibrium points. In the phase portraits, the yaw rate is plotted over the sideslip angle, for each phase portrait the steering angle is held constant.

They also investigate the human behaviour to enter a drift and how to control the car in the drift. They conclude, that an open-loop sequence can be used to bring the “initial” conditions close to one of the drift equilibria. When the states are close enough to one of the drift equilibria, the closed-loop controller can be activated to keep the car in the equilibrium.

Two controllers are designed. The longitudinal controller is supposed to keep the speed at the desired constant value. It uses the velocity error and a gain to calculate the input to the motors. For the steering angle, a state-feedback controller is used.

The performance has been tested on a self-build vehicle with good results. Hence, their choice of the simple bicycle model, the approach of combined open-loop and closed-loop control as well as the choice of the relatively simple controllers is validated.

1.2.4 Tyre modelling

Tyres consists of multiple layers of elastomers, metals and often polyamides, which makes it very difficult to describe their behaviour. Approaches of using the Finite Element Method (FEM) to describe the tyre are usually too complicated for fast computations needed in controllers, therefore other models have to be used in many applications [47].

There are two common classifications of tyre models. The first is to distinguish whether the model is supposed to capture the transient behaviour of the tyre or the steady-state behaviour. The models capturing the transients during braking or accelerating are called dynamical tyre models, e.g., the LuGre and SWIFT model [48]. Steady-state models for constant angular and linear velocities are the HSRI and the Pacejka-model [48].

The other approach of classifying tyre models is to distinguish how the description was derived. Some models purely rely on empirical data to describe the tyre behaviour, for example the Pacejka model, or the ones proposed by Burckhardt, Kinecke and Nielssen [48]. The Pacejka model is also referred to as the magic formula, since there is no physical model involved but it still captures the tyre behaviour. The other approach is to derive a model from basic physical descriptions. Out of these, the brush model approach is described here.

The brush tyre model was invented by Fromm. The contact patch between tyre and road is divided into small beams (brush elements) as shown in Figure 3. These beams are in contact with the ground, the contact patch is divided into an adhesion and a sliding region. In the adhesion region, static friction is assumed, in the sliding region, coulomb friction is used to calculate the forces [48]. It is assumed, that the deformation of the beams is linear, this is clearly an approximation of the nonlinear behaviour of the elastomer.

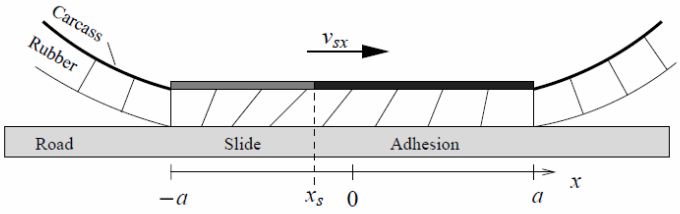

Figure 3: Deformation of the rubber at the contact patch according to the brush model [49].

Fromm assumed a rigid carcass, Fiala altered the model by assuming a flexible carcass. In the Fiala tyre model, the wheel and the tread of the tyre are connected through springs and guides as shown in Figure 4. Both models should only be used for stationary cases.

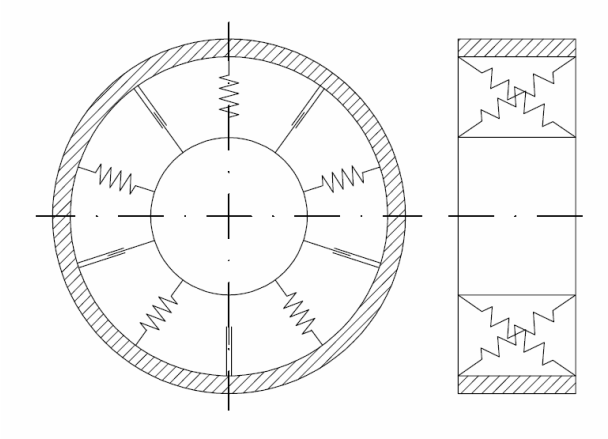

Figure 4: Fiala tyre model [47].

1.3 Linear quadratic regulator

For the Linear Quadratic Regulator (LQR), a cost function is minimized to calculate the optimal gains for a state feedback design. The cost function for the continuous case, (1), is given below in (2). The cost matrices Q, R and N must be designed. These design factors determine the trade-off between punishing state deviations and control input. The optimal gains in the gain matrix K for the chosen cost matrices are then calculated by solving the Riccati equation (3) for P and the solution to the equation (4). The continuous state space model, the cost function, the Riccati equation and the equation for the feedback gains are:

$$\dot{x} = A\,x + B\,u\,, \tag{1}$$

$$J(u) = \int_{t=0}^{\infty} (x^T\,Q\,x + u^T\,R\,u + 2x^T\,N\,u)\;dt\,, \tag{2}$$

$$A^T P + PA - (PB + N)R^{-1}\,(B^{-1}P + N^T) + Q = 0\,, \tag{3}$$

$$K = R^{-1}\,(B^T P + N^T)\,. \tag{4}$$

1.4 Model predictive control

Model Predictive Control (MPC) originated in the 1970's. It uses a model to predict the future states of a system on a predefined horizon. The MPC algorithm performs the following 3 steps in a loop.

1. Sampling of the system states.
2. An optimization function is minimized to obtain the "optimal" inputs for the whole prediction horizon under consideration of the constraints.
3. The first calculated input is applied to the system.

In each step, a prediction of the whole horizon is performed, when the next iteration is performed the prediction horizon reaches one sampling instance further, this is the reason why MPC is also called receding horizon predictive control. Because of the sampling after each iteration, the algorithm is somewhat robust to modelling errors. However, proving robustness and stability can be challenging [50].

One benefit of MPC is, that it can be used for many different systems, from simple to complex dynamics, systems with long delays and unstable systems. It is also possible to use Nonlinear Model Predictive Control (NMPC) for nonlinear systems. Because of the structure of the MPC formulation it is easy for the user to add constraints. These constraints are considered directly by the system, which means that, according to the used model, no input and state combination will be produced that violates these constraints. If it is not possible to find an input that does not violate the constraints, the MPC gets infeasible and no input will be calculated. It is up to the user to define what happens in such a case. By considering the constraints directly, a high potential for increased performance compared to other control methods arises. For example, a PID controller does not account for constraints directly, thus it has to be de-tuned to ensure, that the constraint will never be reached. Or other actions must be taken, when it reaches these constraints.

On the other hand, MPC also has its drawbacks, since an optimization problem has to be solved in each sampling time it is very computationally demanding. There exist good solvers for convex-problem formulations that can ensure to converge in a given time. But for nonlinear problems this can be a strong burden.

The computational demands are the reason why MPC was only used for relatively slow processes in the last decades, for example in the chemical industry. With the rising computational power, MPC found its application in many other fields. In vehicles MPC can be used for applications in the Powertrain, the engine as well as ADAS, like adaptive cruise control [51].

1.5 Experimental platform and environment

The experiments are carried out in the Smart Mobility Lab (SML) at KTH using a vehicle based on the F1/tenth competition vehicles.

The vehicle that is to be controlled is shown in Figure 5. It is build based on the instructions in [52] for the F1/tenth competition, carried out at the University of Pennsylvania. The remote-controlled vehicle is a Traxxas rally [53]. The vehicle is usually 4WD, but the shaft has been removed to achieve a RWD. Furthermore, the original tyres have been replaced by smaller slick tyres with a diameter of 65mm. On the vehicle is a Nvidia jetson GPU, an Inertial Measurement Unit (IMU) and a WIFI access point. Further information about the specifications can be found on the website to the F1/tenth project [52].

In the SML is a six by six meters test space with a smooth floor. In this area, the location and motion of the vehicle can be measured by the Qualisys Motion Capture system (MOCAP), which provides a measurement of 6 degrees of freedom at 120 Hz.

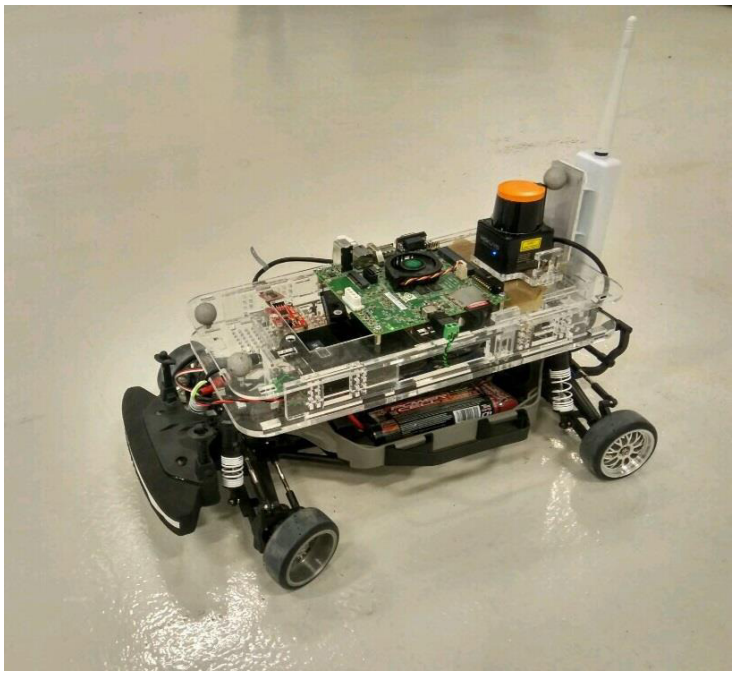

Figure 5: F1/tenth vehicle on the test area.

2 VEHICLE MODELLING

The vehicle is modelled using a bicycle model, as shown in Figure 1, and the empirical Fiala lateral tyre model used in [37].

The used models are described further in 2.1 and 2.2. The procedure for the parameter identification for the empirical Fiala tyre model is described in 2.3. The resulting model is compared to the physical vehicle in 2.4.

2.1 Bicycle model

The vehicle is modeled using a bicycle model with the states lateral velocity v_y and yaw rate r, the only input to the model is the steering angle δ, since the longitudinal velocity v_x is assumed constant. The mass m, the moment of inertia Iz, and the distances between the axles and the centre of gravity (COG) are given in *Table 1*. The state equations are:

$$\dot{v}_y = \frac{F_{y,f}\ \cos\delta + F_{y,r}}{m} - r\ v_x\ , \tag{5}$$

$$\dot{r} = \frac{aF_{y,f}\cos\delta + bF_{y,r}}{I_z}. \tag{6}$$

Distance from COG to front axle	a	0.18	m
Distance from COG to rear axle	b	0.15	m
Vehicle mass	m	3.85	kg
Yaw inertia	I_z	0.06	kg m²
Normal load on front tyre	F_{zf}	17.17	N
Normal load on rear tyre	F_{zr}	20.60	N

Table 1: Parameters for F1/tenth vehicle.

2.2 Tyre model

The lateral tyre forces are calculated with the Fiala tyre model (7):

$$F_{y(\alpha)} = \begin{cases} -C_\alpha \tan\alpha + \dfrac{C_\alpha^2 \left(2 - {\mu_s}/{\mu_p}\right)}{3\,\mu_p F_z} |\tan\alpha| \tan\alpha \\ \dfrac{-C_\alpha^3 \left(1 - {2\mu_s}/{3\mu_p}\right)}{9\mu_p^2 F_z^2} tan^3\alpha, & |\alpha| < \alpha_{sl}\,, \\ -\mu_s F_z\, sgn\,\alpha, & |\alpha| > \alpha_{sl}\,, \end{cases} \tag{7}$$

$$\alpha_{sl} = \tan^{-1}\frac{3\mu_p F_z}{C_\alpha}.$$

The normal load F_{zf}, *and* F_{zr} for the front and rear axle, respectively, are given in Table 1. The peak friction coefficient μ_p and the sliding friction coefficient μ_s between the tyre and the road are assumed to be equal. The friction coefficient μ and the tyre cornering stiffness C_α need to be identified experimentally with the ramp steer manoeuvre. Whereas, the slip angles for the front tyre α_f and for the rear tyre α_r can be calculated with the following equations:

$$\alpha_f = \tan^{-1}\frac{v_y + ar}{v_x} - \delta\,, \tag{8}$$

$$\alpha_r = \tan^{-1}\frac{v_y + br}{v_x}\,. \tag{9}$$

2.3 Parameter identification

As mentioned before, the tyre cornering stiffnesses and the friction coefficients for front and rear tyre of the tyre model need to be identified empirically. It is possible to identify these parameters by fitting a curve to plots of the tyre forces over the slip angles. In this section, it is described how to derive these plots and how to fit the curve to adjust these parameters.

A quasi steady state ramp steer manoeuvre is performed. In this experiment, the vehicle drives in a circle while the steering angle is increased slowly (0.3 deg/s), such that steady state behaviour can be assumed. Under steady state conditions it is possible to approximate the lateral acceleration as in (10):

$$a_y^{ss} = r\, v_x\,. \tag{10}$$

The agreement between the measured and calculated data is shown in Figure 6.

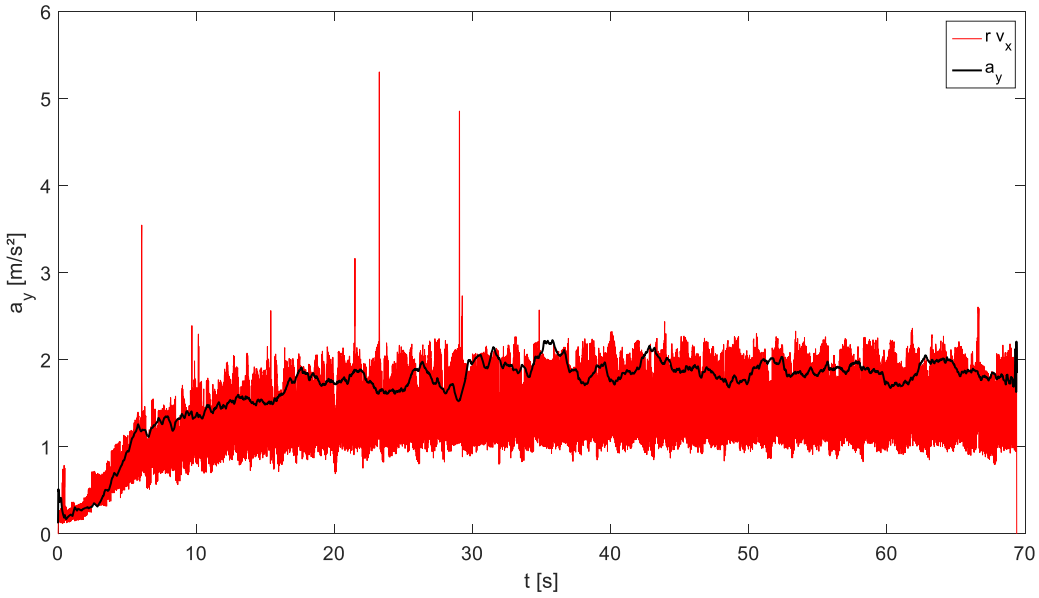

Figure 6: Measured lateral acceleration a_y and approximated lateral acceleration $r\, v_x$.

With (10), and the steady state approximation to the state equations (5) and (6), the tyre lateral forces for the front and the rear tyre can be derived as:

$$F_{y,f} = \frac{mb}{(a+b)\,\cos\delta}\, v_x r = \frac{mb}{(a+b)\,\cos\delta}\, a_y^{ss}\,, \tag{11}$$

$$F_{y,r} = \frac{ma}{a+b}\, v_x r = \frac{ma}{a+b}\, a_y^{ss}\,. \tag{12}$$

During the experiment, the IMU on the vehicle measures the acceleration in x-direction a_x, the acceleration in y-direction a_y, and the angular velocity around the z-axis, the yaw rate r. The MOCAP system measures the position of the vehicle in the test space on the x-axis, and y-axis, x_{pos} and y_{pos}, respectively. Furthermore, the MOCAP measures the orientation of the vehicle around the z-axis, the yaw ψ. These measurements are logged together with the input values for the longitudinal velocity and the steering angle δ. All data is logged with a frequency of 100 Hz.

With the logged position data from the MOCAP, it is calculated in which direction the car is moving, V_{dir}, and with which velocity V. The slip angle β, is calculated by comparing the difference of the measured orientation, ψ of the vehicle and V_{dir}. The velocities in the car frame in x- and y-direction can be calculated with the following geometric correlation:

$$v_x = V \ cos\,\beta\ , \tag{13}$$

$$v_y = V \ sin\,\beta\ . \tag{14}$$

The slip angles for front and rear tyre are calculated with (8) and (9). The tyre forces are calculated with (11) and (12), using the logged input angle δ and the acceleration in y direction, a_y. The tyre forces are plotted over the slip angles in Figure 7 and Figure 8.

Both plots show an increasing tyre force for increasing slip angles and a saturated region for the tyre forces. The friction coefficients can be identified from the saturated region, using the saturation part of the Fiala tyre model (7). The tyre cornering stiffnesses can be identified by fitting the tyre forces of the tyre model to the slope of the measured tyre forces. Since there is no peak clearly visible in the tyre curves, it is justified to assume μ_s and μ_p are equal. The identified parameters are shown in Table 2.

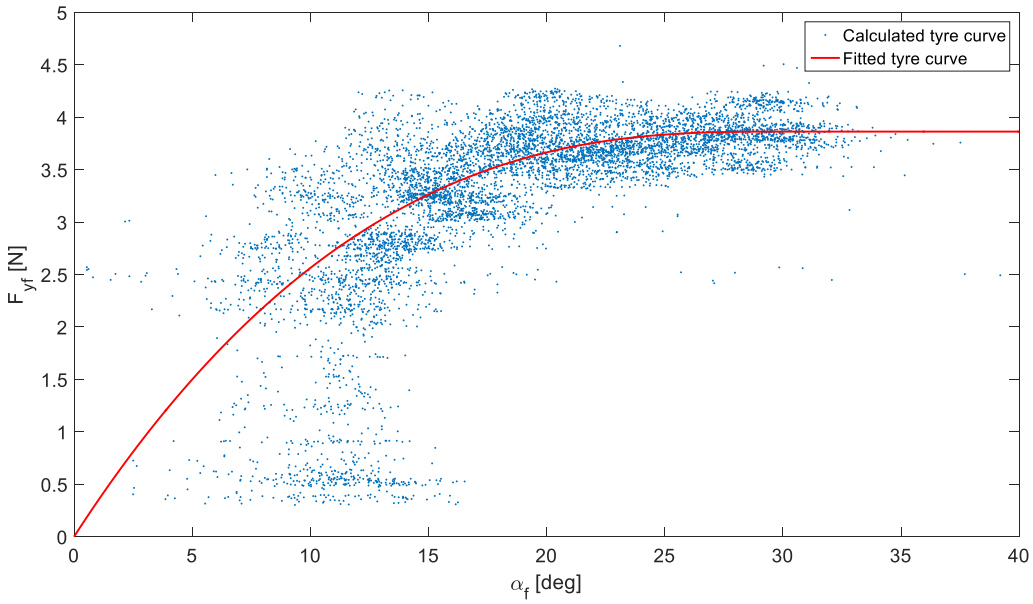

Figure 7: Calculated front tyre force over front tyre slip angle.

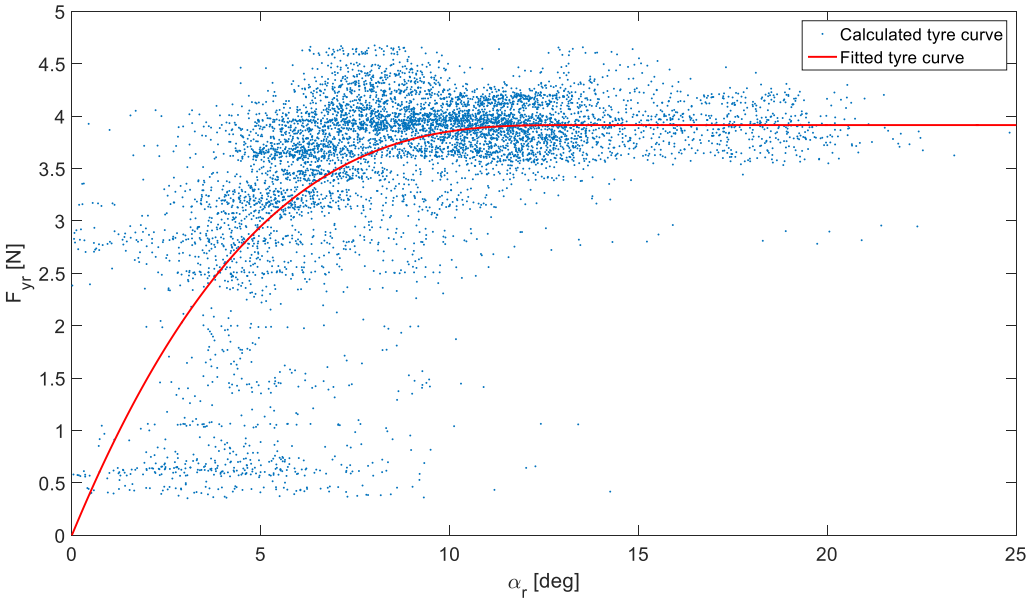

Figure 8: Calculated rear tyre force over rear tyre slip angle.

Front tyre cornering stiffness	$C_{\alpha,f}$	20	N/rad
Rear tyre cornering stiffness	$C_{\alpha,r}$	50	N/rad
Front friction coefficient	μ_f	0.22	-
Rear friction coefficient	μ_r	0.19	-

Table 2: Identified tyre paramters for the Fiala tyre model.

2.3 Parameter verification

To verify the model, measured data from a cornering manoeuvre of the car is compared to a simulation of the model using the same input.

The trajectory of the manoeuvre is shown in Figure 9. The vehicle is positioned at the marked position (black dot) and accelerates on a straight path in positive *x* direction. After approximately 0.5 m the car turns left for a ¾ turn and then abruptly changes the steering angle for a right-hand turn. The steering input is shown in Figure 10. Note that the steering input for the first 0.25 s of the experiments is -0.1 rad (-5.7 deg) and gives a straight movement of the car, as seen in Figure 9.

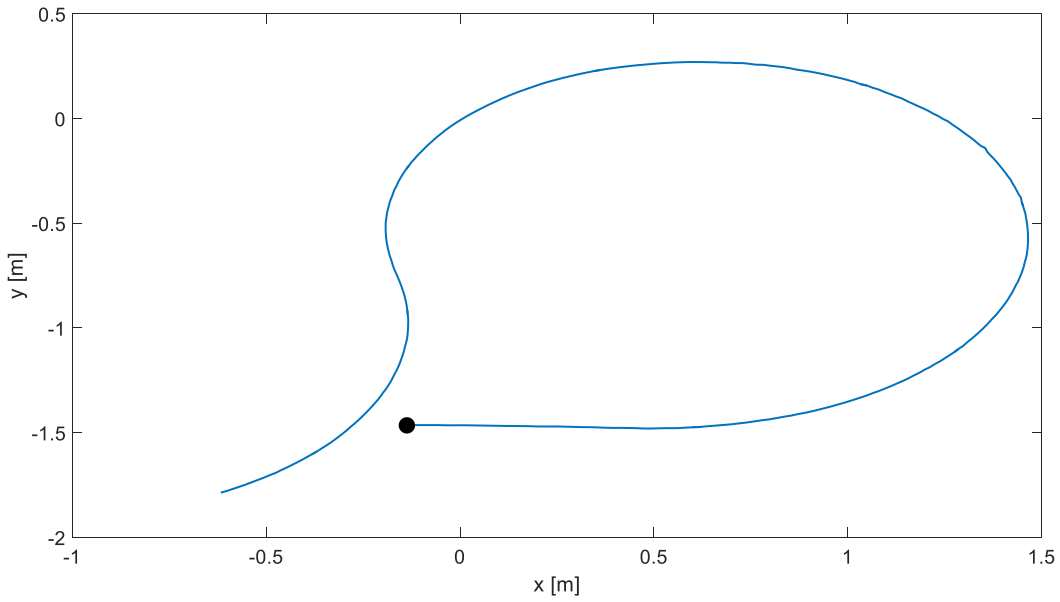

Figure 9: Measured positions during the cornering manoeuvre.

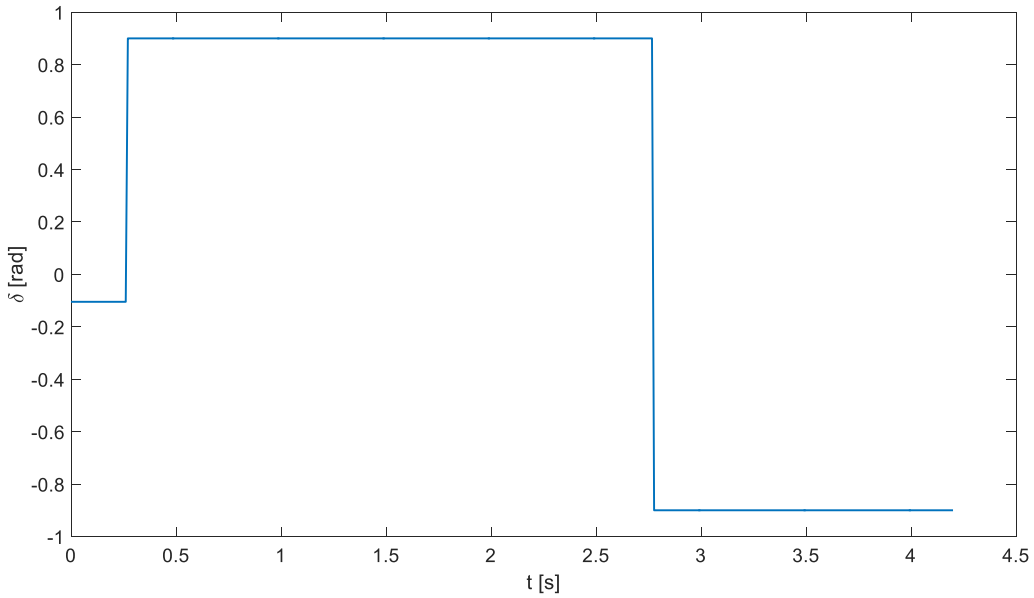

Figure 10: Input steering angle δ during cornering manoeuvre.

The measured and simulated states are shown from Figure 11 to Figure 13. Figure 11 shows a measured lateral velocity of 0.1 m/s for the first 0.5 s, even though the car is driving straight. This could be due to an offset of the IMU. The big overshoots of the simulation can be explained by the sudden massive change in steering angle, the physical car is not able to apply these sudden changes of the steering angle. Furthermore, the overshoot of v_y before decreasing and the undershoot before increasing suggest, that the dynamics of v_y are of non-minimum phase. A scaled plot of the simulated lateral velocity is shown in Figure 12. From this figure, it is evident, that both, the simulation and the measurement give negative lateral velocity for the left-hand turn, and positive lateral velocity for the right-hand turn. However, there is a significant difference in magnitude.

Figure 13 shows the simulated and measured yaw rate of the cornering manoeuvre. In the beginning, the measurement shows a yaw rate of 0, which agrees with driving straight. The simulation shows a negative yaw rate, which is what we expect for a negative input angle. For the left-hand cornering, the simulation and the measurement give a positive yaw rate and for the right-hand cornering both give negative values for the yaw rate. Thus, the qualitative behaviour agrees between simulation and measurement, but the magnitude shows a significant difference.

Both measurements show a big delay between the change of the input and the change of the states. This is partly because the input is logged immediately, but there is a delay when the input is sent to the car and also when the measured data is sent to be logged. Furthermore, the physical car will not be able to apply the sudden changes in the input which will cause further delays.

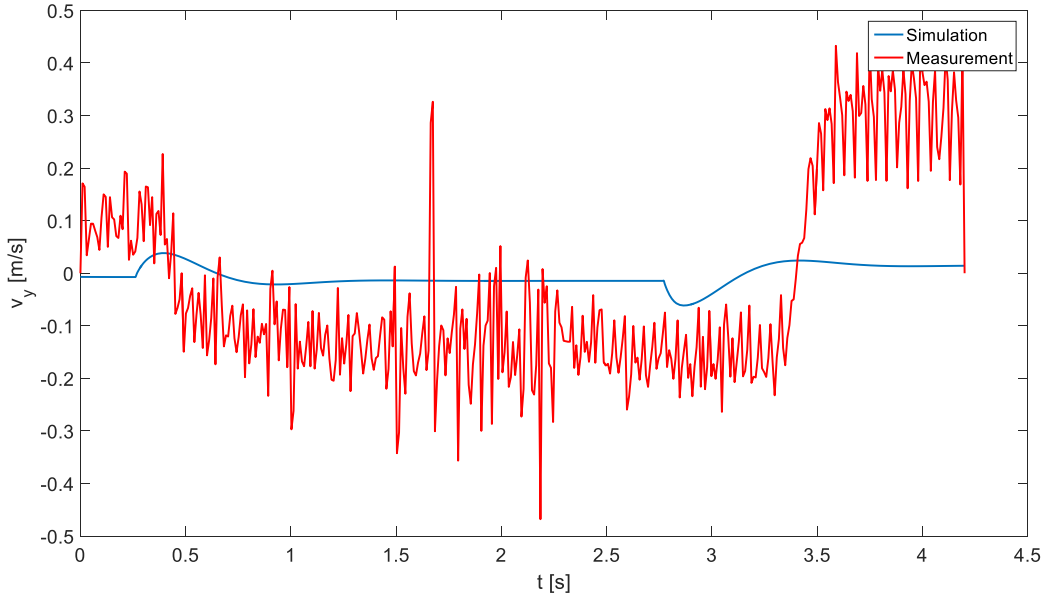

Figure 11: Simulated and measured lateral velocity.

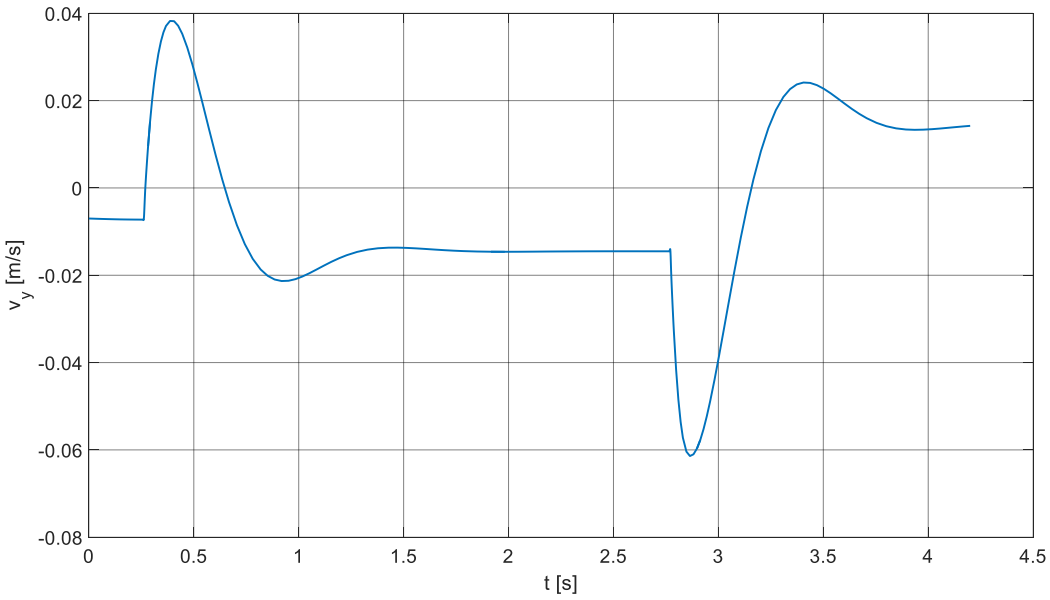

Figure 12: Simulated lateral velocity.

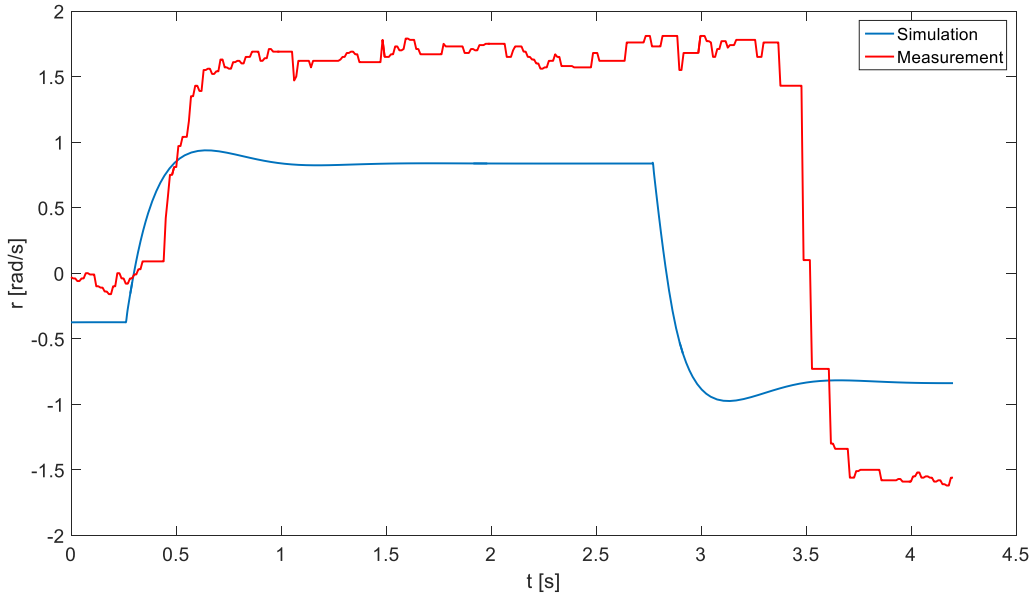

Figure 13: Simulated and measured yaw rate.

The simulation results give some insight to the behaviour of the car during the cornering experiment. For the small negative steering input in the first 0.25 s, it gives a negative yaw rate and a negative lateral velocity. This corresponds to a right-hand cornering. For the steering input of 0.9 rad between 0.25 s and 2.75 s the simulation gives a positive yaw rate and a negative lateral velocity. This corresponds to a left-hand drift equilibrium. For the negative steering input -0.9 rad after 2.75 s, a negative yaw rate and a positive lateral velocity is predicted, this corresponds to a right-hand drift.

3 SYSTEM ANALYSIS

The equilibria of the modelled F1/tenth vehicle are investigated, following the approach in [37]. The equilibria of the system are identified for a range of δ. Afterwards the system behaviour around some equilibria is analysed further, using phase portraits.

3.1 Equilibrium analysis

The sustained drift corresponds to steady state cornering. Therefore, the state equations (5) and (6) can be simplified to (16) and (17) for the steady state case. When the longitudinal velocity v_x^{eq} and the steering input δ^{eq} are kept constant, the system of (16) and (17) can be solved for v_y^{eq} and r^{eq}. Whereas, v_x^{eq} will be kept at $v_x^{eq} = 1.5$ m/s for all calculations, δ^{eq} will be varied over a long range. This provides all steady state equilibria of the system. The equations for the slip angle and the state equations for the steady state case are:

$$\beta = \tan^{-1}\frac{v_y}{v_x}, \tag{15}$$

$$\frac{F_{y,f}\ cos\,\delta + F_{y,r}}{m} - r\,v_x = 0\,, \tag{16}$$

$$\frac{aF_{y,f}\,cos\,\delta + bF_{y,r}}{I_z} = 0\,. \tag{17}$$

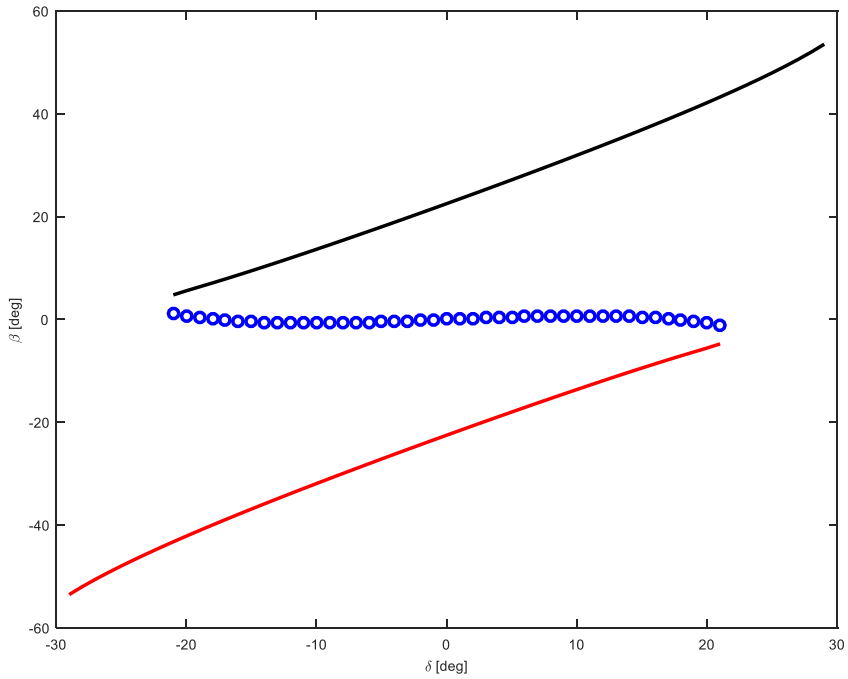

Figure 14: Slip angle β over steering angle δ.

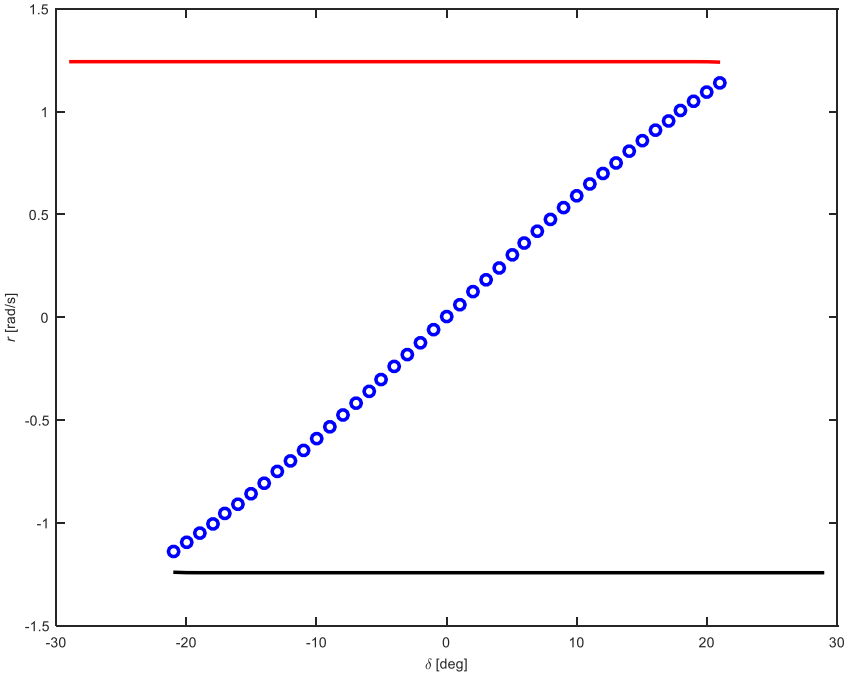

Figure 15: Equilibrium state r over steering angle δ.

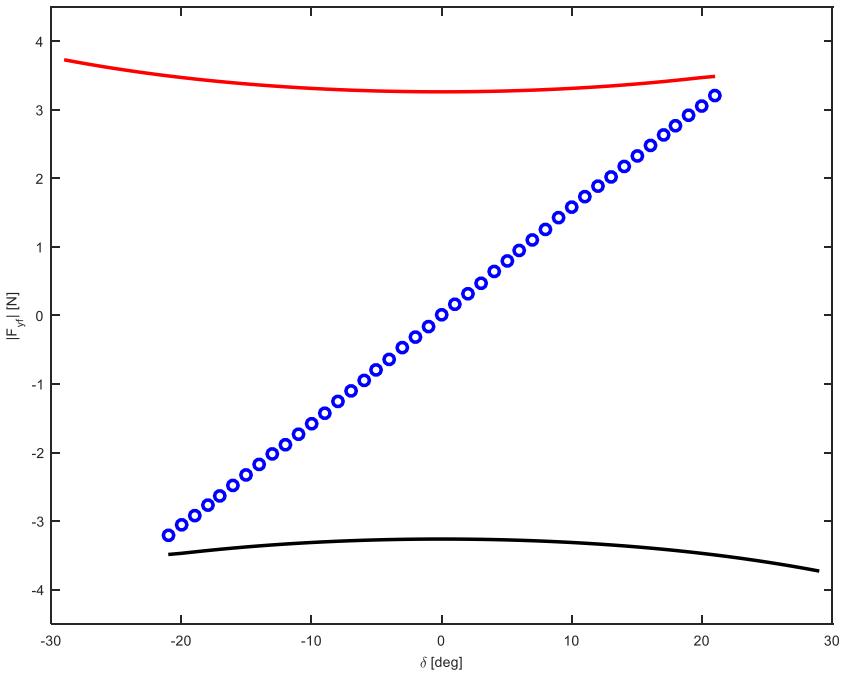

Figure 16: Equilibrium front tyre force F_{yf} over steering angle δ.

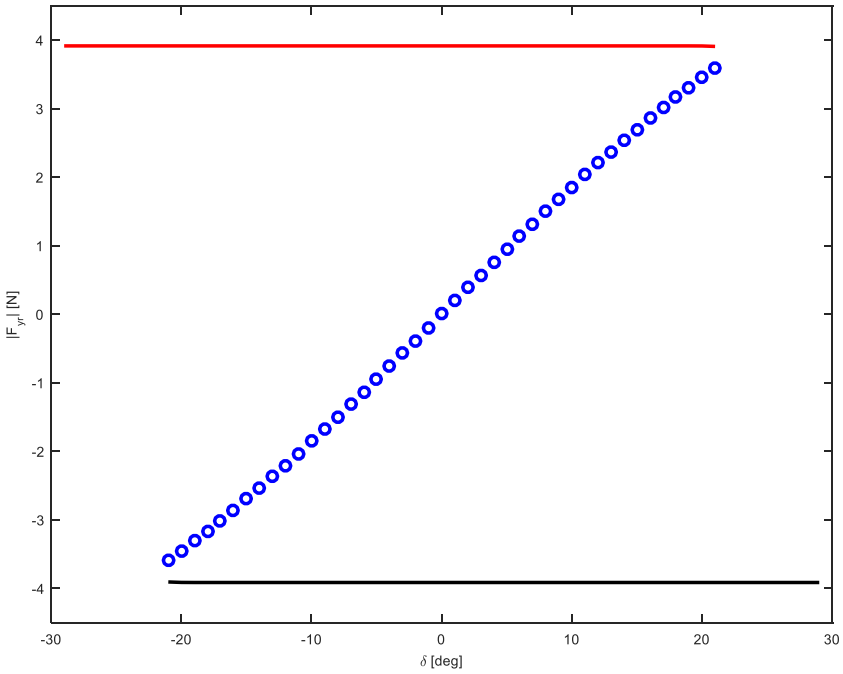

Figure 17: Equilibrium rear tyre force F_{yr} over steering angle δ.

Figure 14 and Figure 15 show the slip angle and the equilibrium state r for varying δ. The slip angle can be calculated from v_x and v_y with (15). Figure 16 and Figure 17 show the corresponding tyre forces. These plots show, that the system contains multiple equilibria for $\delta^{eq} \in$ [-20, 20] deg. Outside of this region exists only one equilibrium for each δ.

The blue dotted part of the plots corresponds to cornering without drifting. In this region, the slip angle is small and the yaw rate increases with increasing steering input. Furthermore, the lateral tyre forces are changing linearly with the steering angle, which indicates cornering within the limits of handling.

The solid lines correspond to the equilibria with saturated rear later tyre force and nearly saturated front lateral tyre force. Here r is almost constant over a long range of δ, whereas β changes significantly with δ. In Figure 14, the red solid line contains $\beta \in$ [-60, -20] deg, for negative δ. Figure 15 shows positive r for negative δ, this corresponds to counter steering. The saturated rear tyre force, high sideslip angle and the counter steer indicate the drift equilibria. The drift equilibria on the red line are left hand drift equilibria, as indicated by the positive yaw rate.

Similar reasoning can be used for the right-hand drift equilibria on the black solid line.

3.2 Phase portraits

The equilibrium analysis only provides the equilibria, but cannot show the behaviour of the system around these. To gain insight into the systems behaviour around the equilibria, phase portraits are used. The phase portraits are plotted for v_x = 1.5 m/s and each phase portrait is plotted for a constant δ.

Figure 18 shows the phase portrait for δ = 0 deg. The same three equilibria can also be seen in Figure 14: Slip angle β over steering angle δ.Figure 14 and Figure 15 for the steering angle of δ = 0 deg.

The equilibrium at the origin, marked with a square, corresponds to driving straight. The trajectories around this point converge to it, this shows, that it is a stable equilibrium. The equilibrium in the top left, marked with a diamond, is a left-hand drift equilibrium. The diverging trajectories show, that this equilibrium is an unstable saddle point. The equilibrium at, marked with a circle, is a right-hand drift equilibrium with the same properties as the other drift equilibrium.

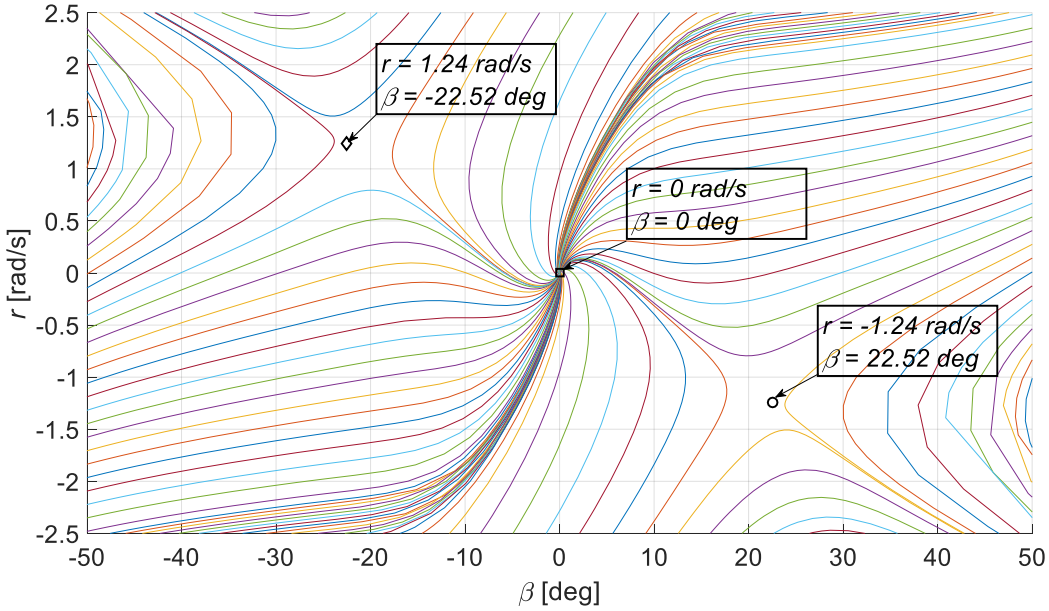

Figure 18: Phase portrait for δ = 0 deg.

Figure 19 shows the phase portrait for a constant δ = -10 deg, so the front tyre is turned to the right. The stable equilibrium, square, is now located at β = -0.73 deg, r = -0.59 rad/s. The negative yaw rate shows, that this corresponds to a right-hand cornering, which is to be expected for a negative δ. The slip angle β increased, compared to Figure 18. The left-hand drift equilibrium, diamond is now located at β = -31.93 deg, r = 1.24 rad/s. Compared to Figure 18, the slip angle became more negative, while the yaw rate remained constant. The right-hand drift equilibrium, circle, also kept the same yaw rate, while the slip angle became more negative.

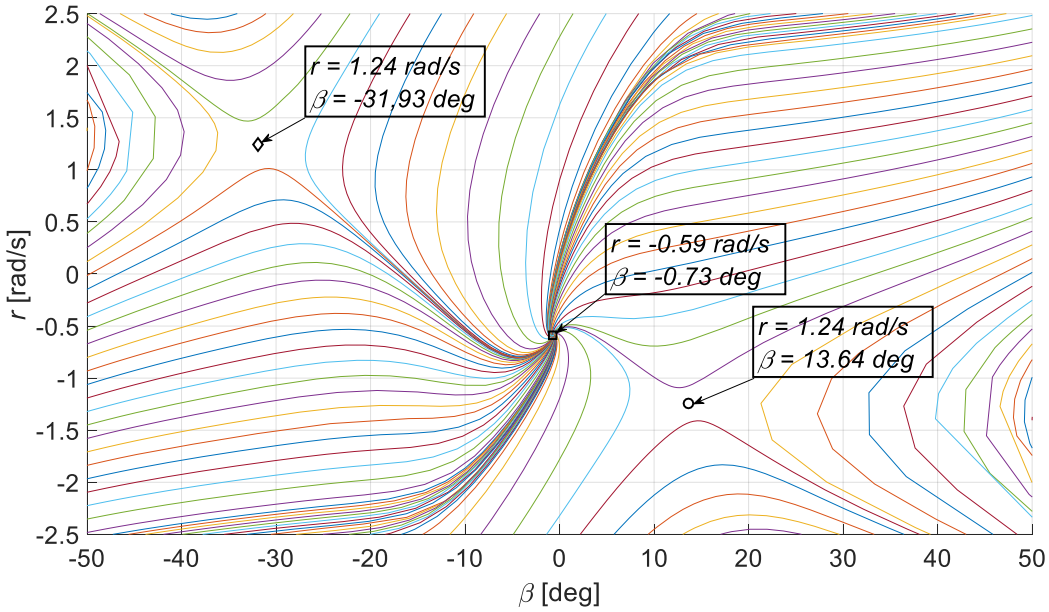

Figure 19: Phase portrait for δ = -10 deg.

The trends of the drift equilibria moving to the left and the stable equilibrium moving down continues for further increasing steering angles, as it can be seen in Figure 20 for δ = -20 deg. This trend continues until the stable equilibrium and the right-hand drift equilibrium, marked with square and circle respectively, collide and vanish. Figure 21 shows the phase portrait for δ = - 25 deg, it only contains the unstable left-hand drift equilibrium, diamond, which is now located at β = -47.97 deg, r = 1.24 rad/s. In Figure 14 and Figure 15 it is also visible, that for δ = - 25 deg only one equilibrium exists. This equilibrium is chosen as the desired drift equilibrium, because the only possible stable cornering for this steering input is a sustained drift.

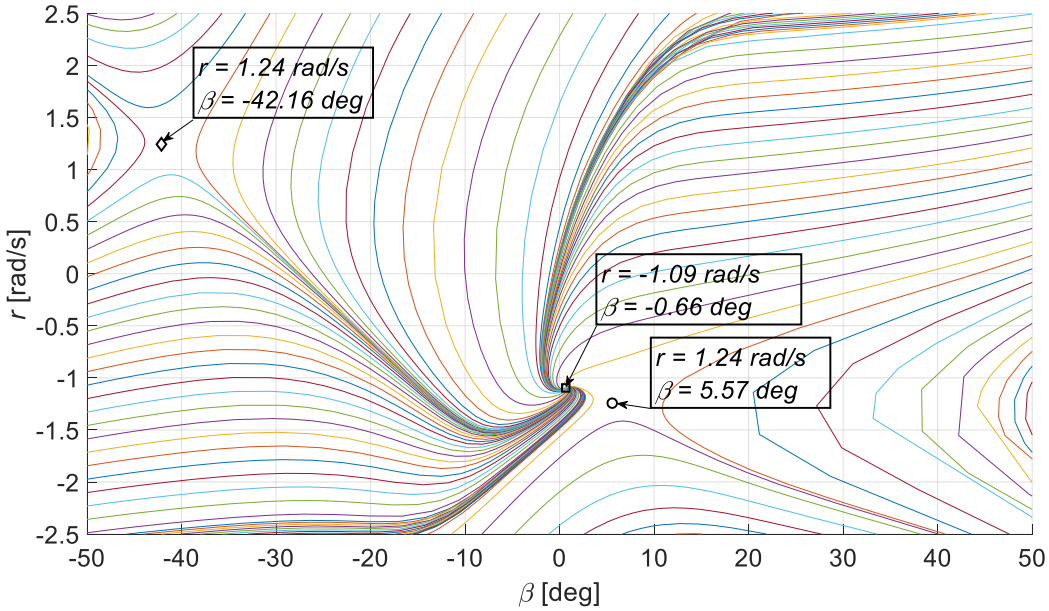

Figure 20: Phase portrait for δ = -20 deg.

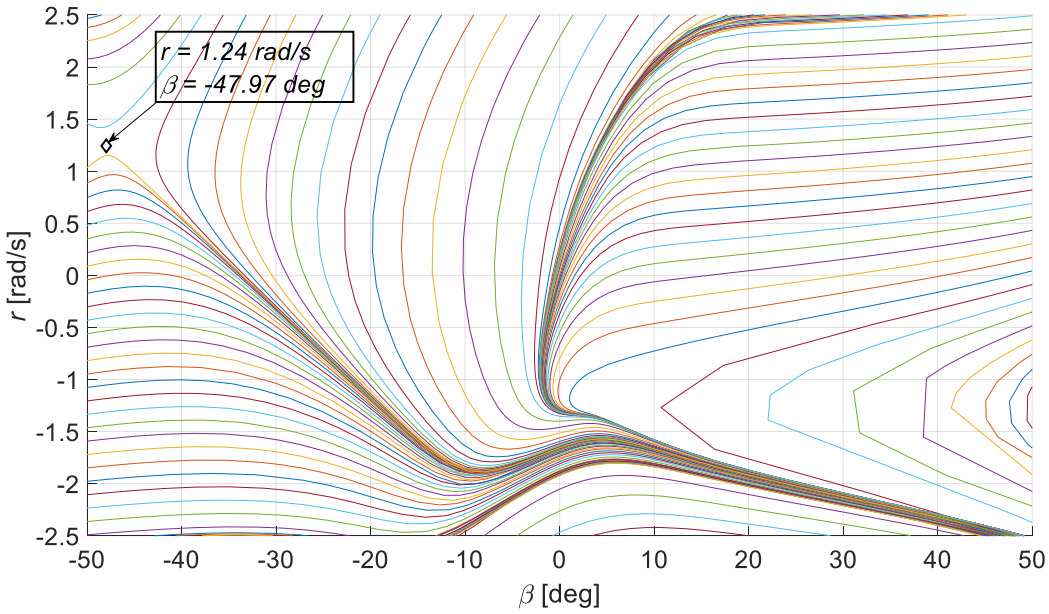

Figure 21: Phase portrait for δ = -25 deg.

4 CONTROLLER DESIGN

As shown in the previous section, the drift equilibria are unstable. For a sustained drift at one of the steady state equilibria, it is necessary to stabilize the system with a controller. The system is linearized around the sole equilibrium shown in Figure 21, the parameters of that equilibrium are listed in Table 3. In this part, a linearized state space model is derived and different controllers are designed to control it around the equilibrium. The system linearization and the design of the feedback gains for the state feedback controller follow the approach in [37]. Subsequently, the feedback gains are calculated using an LQR to improve the performance of the controller. Afterwards a MPC controller is designed to further increase the performance in presence of input-constraints.

The longitudinal velocity is assumed to be constant and is not controlled.

Longitudinal velocity	v_x^{eq}	1.5	m/s
Lateral velocity	v_y^{eq}	-1.66	m/s
Slip angle	β^{eq}	-0.84	rad
		-47.97	deg
Steering angle	δ^{eq}	-0.44	rad
		-25	deg
Yaw rate	r^{eq}	1.24	rad/s

Table 3: Parameters for desired drift equilibrium.

4.1 System linearization

A continuous state space model on the form of (18) is derived by the linearization around the equilibrium in Table 3. The matrices A_c and B_c are calculated in line with (20). Where $\Delta\delta = \delta - \delta^{eq}$, $\Delta v_y = v_y - v_y^{eq}$, $\Delta r = r - r^{eq}$. Furthermore, the continuous state space system is discretized with a sampling time of $T_s = 0.01$ s, to get a discrete system on the form (19). The state space equations for the continuous and the discrete case as well as the matrices A_c and B_c are given as follows:

$$\Delta\dot{x} = A_c\,\Delta x + B_c\,\Delta u\,, \tag{18}$$

where $\Delta x = \begin{bmatrix}\Delta v_y \\ \Delta r\end{bmatrix}$ and $\Delta u = \Delta\delta$,

$$x_{k+1} = x^{eq} + A_d\,\Delta x_k + B_d\,\Delta u_k\,, \tag{19}$$

where $x^{eq}{}_k = \begin{bmatrix}v_{y\,k}^{eq} \\ r^{eq}{}_k\end{bmatrix}$, $\Delta x_k = \begin{bmatrix}\Delta v_{y\,k} \\ \Delta r_k\end{bmatrix}$, and $\Delta u_k = \Delta\delta_k$,

$$A_c = \begin{bmatrix}\frac{d}{dv_y} f_1(v_y, r, \delta) & \frac{d}{dr} f_1(v_y, r, \delta) \\ \frac{d}{dv_y} f_2(v_y, r, \delta) & \frac{d}{dr} f_2(v_y, r, \delta)\end{bmatrix}_{v_y^{eq}, r^{eq}, \delta^{eq}}, \tag{20}$$

$$B_c = \begin{bmatrix}\frac{d}{d\delta} f_1(v_y, r, \delta) \\ \frac{d}{d\delta} f_2(v_y, r, \delta)\end{bmatrix}_{v_y^{eq}, r^{eq}, \delta^{eq}}.$$

The linearization leads to the following continuous state space system. The eigenvalues of the linearized system support the findings in the system analysis, since one positive and one negative eigenvalue correspond to an unstable saddle point:

$$\dot{x} = \underbrace{\begin{bmatrix}-10.59 & -3.377 \\ -122.5 & -21.72\end{bmatrix}}_{A_c}\begin{bmatrix}\Delta v_y \\ \Delta r\end{bmatrix} + \underbrace{\begin{bmatrix}32.42 \\ 375\end{bmatrix}}_{B_c}\Delta\delta\,,$$

$$eig(A_c) = \begin{bmatrix}4.9343 \\ -37.2432\end{bmatrix}.$$

The continuous system is discretised using the zero-order-hold method, it is given below. Note that one of the eigenvalues is outside of the unit circle:

$$x_{k+1} = \begin{bmatrix} v_y^{eq} \\ r^{eq} \end{bmatrix} + \underbrace{\begin{bmatrix} 0.9175 & -0.02895 \\ -1.05 & 0.8221 \end{bmatrix}}_{A_d} \begin{bmatrix} \Delta v_y \\ \Delta r \end{bmatrix} + \underbrace{\begin{bmatrix} 0.2525 \\ 3.214 \end{bmatrix}}_{B_d} \Delta\delta \,,$$

$$eig(A_d) = \begin{bmatrix} 1.0506 \\ 0.6890 \end{bmatrix}.$$

4.2 State feedback-controller

The steering control law is given in (21). Since the system is linearized around δ^{eq}, the steering input is calculated by adding the feedback to this equilibrium input. The feedback gains can be expressed in the gain matrix K = [K_{vy} K_r]. To achieve closed-loop stability of the continuous system, the eigenvalues of the closed loop system A –BK must have a negative real part. With (22) an upper bound on K_{vy} can be calculated, when a K_{vy} is chosen, a lower bound on K_r can be calculated which guarantees closed loop stability. The notation A_{ij} and B_i in (22) correspond to the elements in the matrices A_c and B_c. According to these boundaries, stabilizing gains are chosen. Relatively low gains are chosen to avoid aggressive behaviour which would lead to a fast saturation of the steering input. The gains and the achieved closed loop eigenvalues for the discrete system are shown in Table 4. The eigenvalues inside the unit circle show that the closed loop system is now stable. The stable behaviour around the equilibrium point can also be seen in the phase portrait of the closed loop system, Figure 22. This plot also shows that the CL-system contains another stable equilibrium. The control law for the steering angle and the boundaries of the gains are:

$$\delta = \delta^{eq} + \Delta\delta = \delta^{eq} - K_{vy}\Delta v_y - K_r \Delta r \,, \tag{21}$$

$$K_{vy} < K_{vy,crit} = \frac{\det(A)\, B_2 - (B_2 A_{11} - A_{21} B_1) trace(A)}{B_1 B_2 trace(A) - A_{12} B_2^2 - A_{21} B_1^2}, \tag{22}$$

$$K_r > K_{r,crit} = \frac{trace(A) - B_1 K_{vy}}{B_2}.$$

Feedback gains	K_{vy}	-0.65	rad/m
	K_r	0.18	rad
Eigenvalues of the discrete CL-system		0.98	
		0.36	

Table 4: Feedback gains and closed loop eigenvalues for the SF-controller.

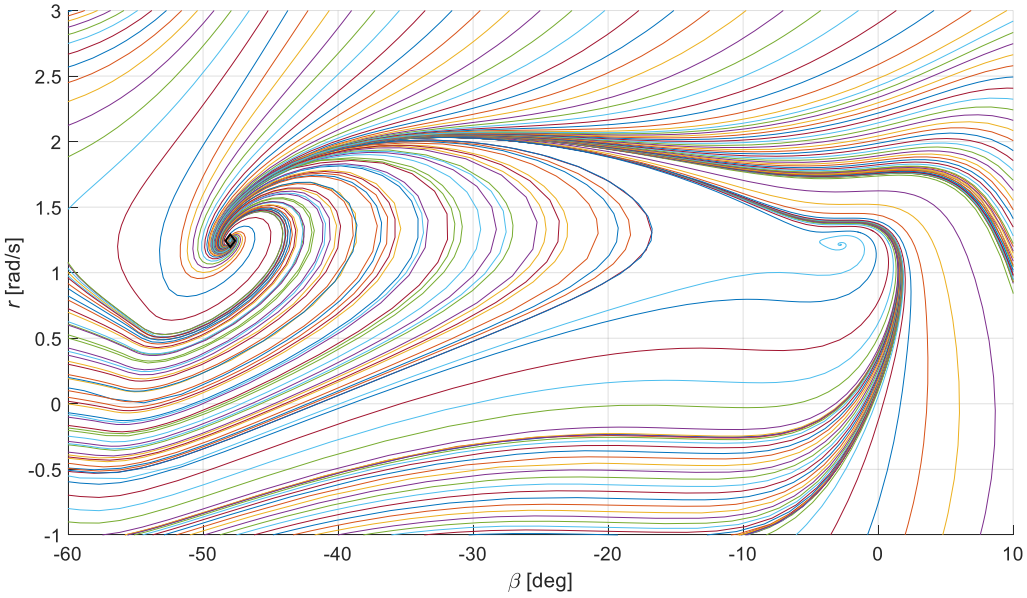

Figure 22: Phase portrait of the closed loop system with SF gains.

4.3 LQR-controller

In order to improve the state feedback controller, the feedback gains will be generated using the LQR approach. The calculated feedback gains and the resulting eigenvalues are shown in Table 5. Figure 23 shows the phase portrait of the closed loop system. It shows that the trajectories in the vicinity of the desired equilibrium converge to it. It also shows a region of attraction around the second equilibrium. Note, that some initial conditions have been added for r = 1 rad/s and $\beta \in$ [-51 -40] to show the behaviour around the equilibrium better. The cost function (23) and the following matrices are used for the controller design for the discretized state feedback system:

$$J(u) = \sum_{n=1}^{\infty} \left(\Delta x_k{}^T \, Q \, \Delta x_k + \Delta u_k{}^T \, R \, \Delta u_k + 2 \Delta x_k{}^T \, N \, \Delta u_k \right), \tag{23}$$

where

$$Q = \begin{bmatrix} 1 & 0 \\ 0 & 1 \end{bmatrix}, R = 0.1, N = 0 \, .$$

Feedback gains	K_{vy}	-0.63	rad/m
	K_r	0.28	rad
Eigenvalues of the discrete CL-system		0.98	
		0.0069	

Table 5: Feedback gains and closed loop eigenvalues for the LQR-controller.

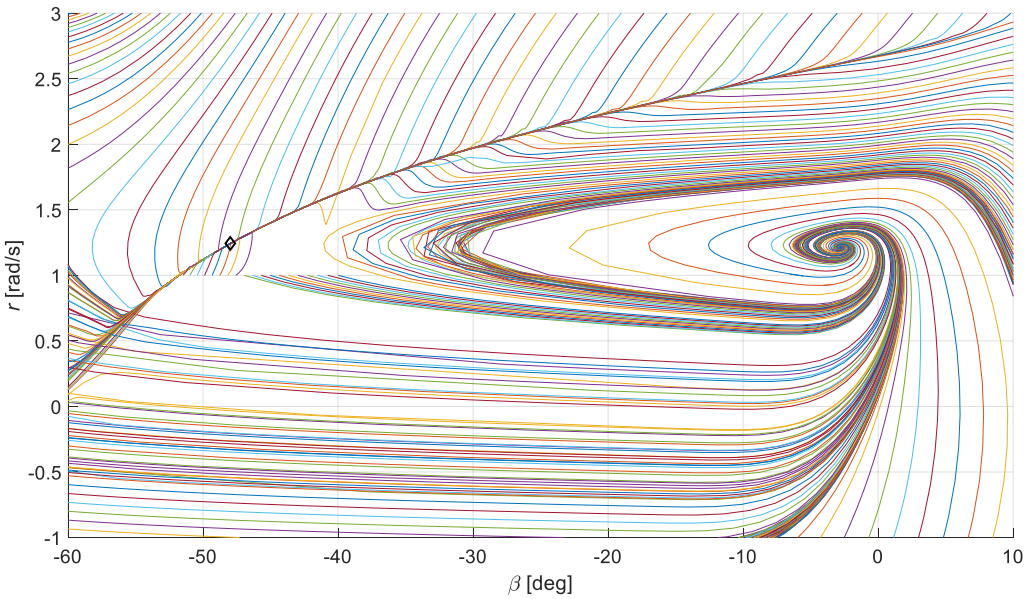

Figure 23: Phase portrait of the closed loop system with LQR gains.

4.3 MPC-controller

A MPC controller is designed to make the system more robust when the boundaries on the steering rate and steering input are reached. The cost function for the MPC and the cost matrices are given in (24). S corresponds to the maximal steering rate of 20 deg/s and u_{max} gives the maximal steering angle δ of 34.37 deg. The cost matrix on the final states Q_f is chosen to be the solution to the Riccati equation of (23). This guarantees that the solution of the unconstrained MPC and the LQR are equal. The prediction horizon is N = 20. Figure 24 shows the phase portrait of the CL-system, it shows that the controller stabilizes the system around the equilibrium. The second equilibrium is also apparent in this phase portrait. The cost function, cost matrices and the boundaries are:

$$J(x(t)) = \underset{u_1, u_2, \dots\, u_{N-1}}{minimize} \sum_{k=0}^{N-1} \Delta x_k{}^T\, Q\, \Delta x_k + \Delta u_k{}^T\, R\, \Delta u_k + \Delta x_N{}^T\, Q_f\, \Delta x_N, \tag{24}$$

subject to

$$\begin{gathered} x_{k+1} = x^{eq} + A_d\, \Delta x_k + B_d\, \Delta u_k \\ x_0 = x(t) \\ |u_k| < u_{max} \\ |u_k - u_{k-1}| < S \end{gathered} \quad ,$$

where

$$Q = \begin{bmatrix} 1 & 0 \\ 0 & 1 \end{bmatrix}, R = 0.1, \qquad Q_f = \begin{bmatrix} 74.3502 & -6.8750 \\ -6.8750 & 1.6494 \end{bmatrix},$$
$$u_{max} = 0.6\, rad, S = 0.003491\, rad\,.$$

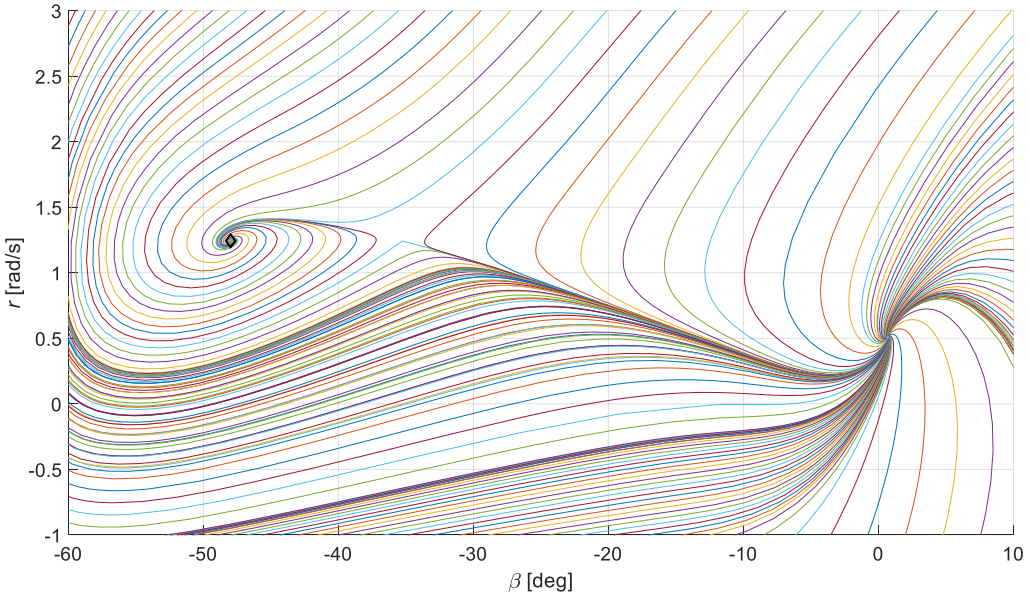

Figure 24: Phase portrait of the closed loop system with the MPC controller.

5 PERFORMANCE EVALUATION

The system is simulated with the 3 different controllers to evaluate the performance. The initial conditions for the simulation are x_{init} = [-1.5 1.4], for $t \in$ [5 5.5] s a disturbance acts on the front tyre friction coefficient and decreases it from $\mu_f = 0.22$ to $\mu_f = 0.17$. A decreased friction coefficient between tyre and underground could be caused by dirt or oil on the ground.

Figure 25 shows the steering angle δ of the 3 controllers during the experiment. It is visible that all δ go to δ^{eq} after the system reached its equilibrium. When the disturbance is introduced at t = 5 s, all δ increase with the maximal steering rate, where the MPC input is slightly delayed. The steering rate of the MPC decreases after t = 5.8 s, while the other inputs increase further with the maximal rate. After t = 6 s the steering angle of the SF and the LQR controller decrease with the maximal rate, while the MPC controller input decreases gentler. After a small undershoot at t = 8 s, the MPC input settles at δ^{eq}. Both of the other controllers inputs decrease until they hit the lower bound u_{max}. After another over- and undershoot the LQR steering angle settles at δ^{eq}. The SF controller input does not converge to δ^{eq}, even for longer simulation times.

Figure 26 and Figure 27 show the states v_y and r, respectively. All controllers manage to bring the system to the equilibrium from the initial conditions. The LQR and the MPC controller show very similar performance, while the SF controller produces a stronger over- and undershoot of r. When the friction on the front tyre is decreased, the amplitude of the yaw rate and the lateral velocity decrease until the car is almost driving straight. All controllers succeed to stop this trend after the disturbance is removed at t = 5.5 s. The LQR controller and the MPC controller manage to bring the system to the equilibrium, while the SF controller does not. The MPC controller produces a slightly higher overshoot in v_y compared to the LQR controller. Otherwise, it gives better results in terms of overshoot, undershoot and settling time, as it is shown in Table 6 and Table 7. The overshoot and undershoot are calculated relative to the equilibrium values. The settling time is the time until the state is within a ±5 % window around the equilibrium value after the disturbance is removed at t = 5.5 s.

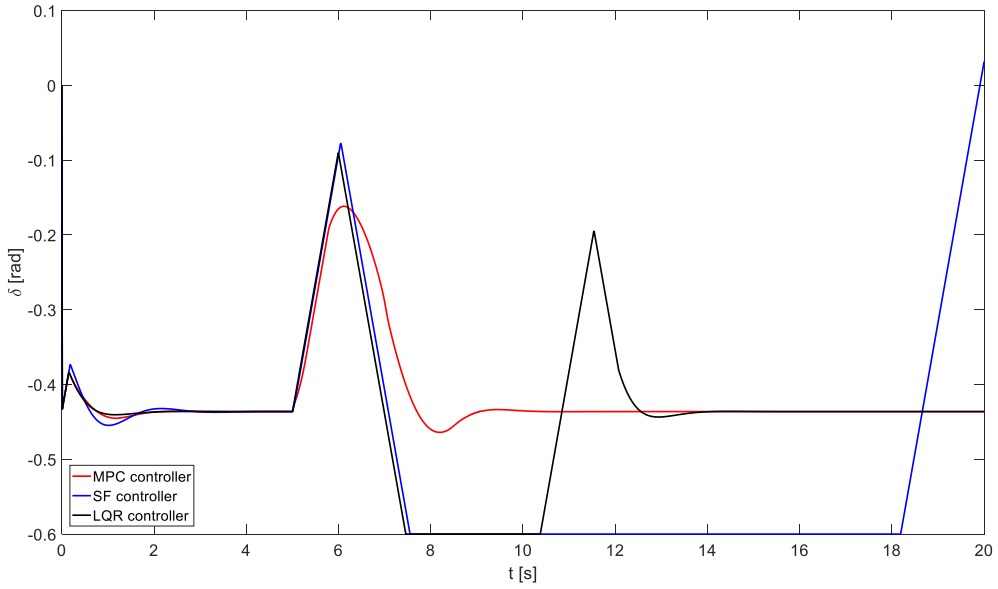

Figure 25: Steering angles of the 3 controllers during the simulation.

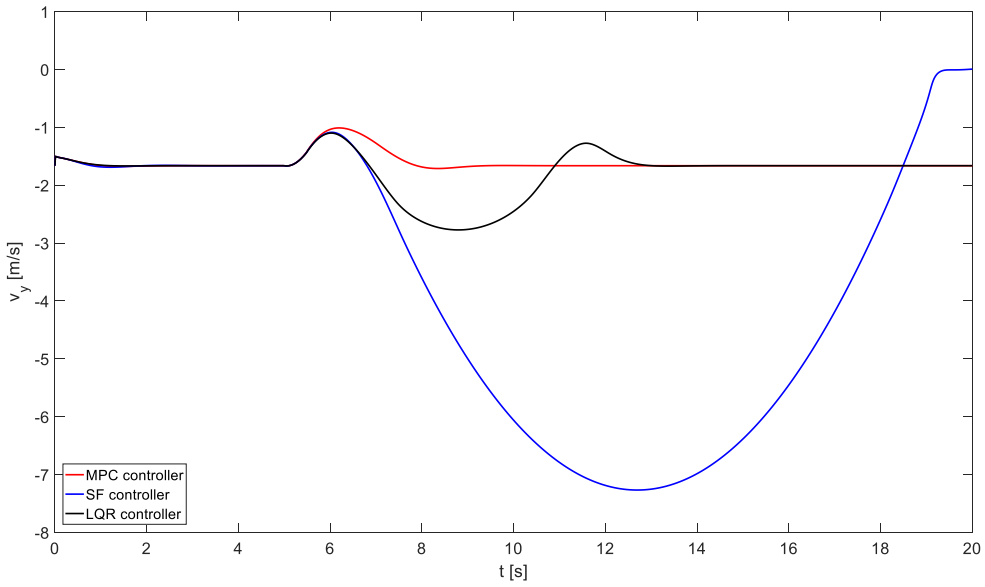

Figure 26: Lateral velocity v_y during the simulation of the 3 controllers.

LQR controller	overshoot	34	%
	undershoot	67	%
	settling time	6.93	s
MPC controller	overshoot	39	%
	undershoot	2.9	%
	Settling time	2.12	s

Table 6: Simulation results for v_y after disturbance is removed at 5.5s.

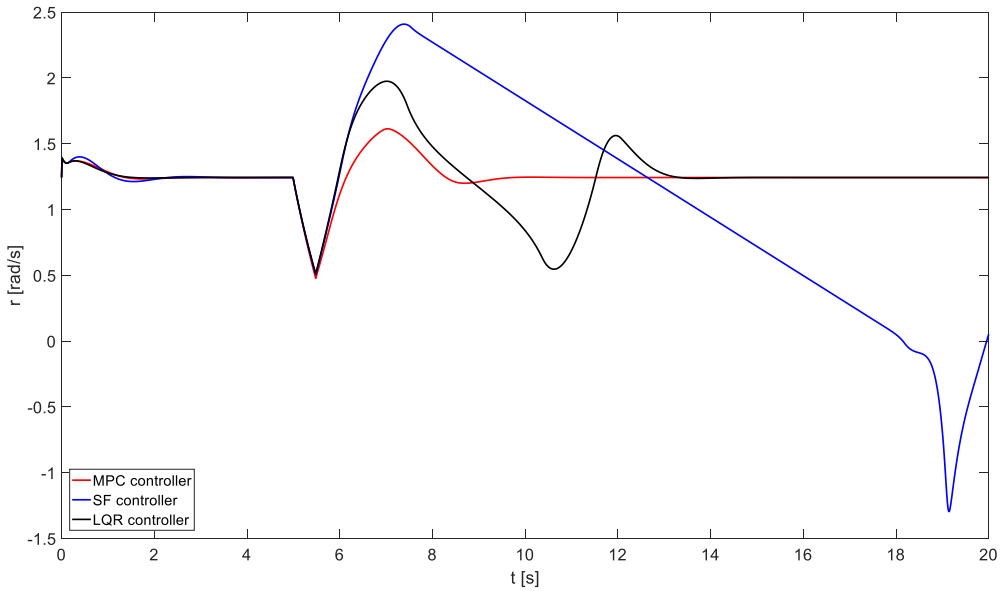

Figure 27: Yaw rate r during the simulation of the 3 controllers.

LQR controller	overshoot	59	%
	undershoot	56	%
	settling time	7.30	s
MPC controller	overshoot	30	%
	undershoot	3.5	%
	Settling time	2.60	s

Table 7: Simulation results for r after disturbance is removed at 5.5s.

6 CONCLUSIONS AND FUTURE WORK

In this part, the results are discussed in respect to the goals of the thesis and conclusions are derived. Additionally, possibilities to build up on the results for future work are presented.

6.1 Conclusions

The conclusions about the modelling, simulation and the planned implementation are presented in this section.

6.1.1 Modelling

The parameter verification in section 2.3, revealed a significant difference between the measured data and the results of the simulation. This can be partly explained by the simplification of the vehicle, using the bicycle model as well as the simplifications in the tyre modelling. Furthermore, the parameter identification itself may lead to some errors, especially the following points can have an influence on the parameter identification:

- The high noise level of the IMU leads to the wide range of the tyre forces in Figure 7 and Figure 8. The time delay, which is obvious from the verification experiment, can lead to unsynchronised data of the MOCAP, input, and the data from the vehicle. This can have an influence on the calculations for the tyre forces. However, since the ramp steer manoeuvre is performed close to steady state conditions, this influence is minimized.

- For the ramp steer manoeuvre, the input for the longitudinal velocity v_x was held constant. Since this experiment should be performed with a constant velocity, it would be beneficial to use a controller to achieve a constant velocity by varying the input. To minimize the influence of the varying velocity on the parameter identification, the calculated actual velocity of the vehicle is used.

Additionally, the experiment used for the parameter verification only achieves a measured slip angle β below 6 deg. Since the slip angle of the desired equilibrium is β = 48 deg it would be beneficial to have verification experiments with higher slip angles.

On the other hand, the identified parameters agree with the parameters in [37] in that sense, that the rear tyre cornering stiffness is significantly higher than the front tyre cornering stiffness and the ratios between the friction coefficients are similar. The magnitude of the tyre cornering stiffnesses agrees with the ones of a similar vehicle in [41]. Furthermore, the results of the stability analysis agree qualitatively with the results in [37]. Several simulations with different input sequences were performed to verify that the simulation gives the expected results. These simulations were performed for different slip angles, some of the experiments were compared to experiments with the vehicle. From the simulations, the qualitative correct behaviour of the car could be confirmed.

This leads to the conclusion, that the modelling should be improved before implementation attempts are made. Since [37], [43], [35], [44], [45], and [46] showed that a simple bicycle model and simple models for the tyre forces are sufficient for implementation, the improvement of the

model should be achieved by improving the parameter identification. A good identification of parameters should be verified by further experiments with higher slip angles.

6.1.2 Simulation

The simulation in section 5, presented increasing performance from SF controller to the LQR controller and the best performance for the MPC controller. The experiment resembles a decrease of friction on the front tyres, which can be due to dirt or other changing conditions on the ground. To sustain a drift, it is important that the controller is able to keep the vehicle close to the equilibrium while these disturbances act on the system. Several simulations with different disturbances on the friction of the front and rear tyre were performed. They showed better performance of the LQR controller compared to the SF controller. However, the MPC controller only performed better than the LQR controller when the input reached the boundaries, as it is to be expected. With the wide range of possible input and higher expected steering rate on the vehicle, the LQR controller will achieve the same results as the MPC for many disturbance scenarios.

6.1.3 Implementation

However, another important factor to achieve the sustained drifting is the robustness to deviating initial conditions, since the vehicle has to be brought close to the equilibrium state before the controller can be activated. From the phase portraits of the closed loop systems with the different controllers, Figure 22, Figure 23, and Figure 24, it is visible that the SF controller has the biggest region of attraction around the desired equilibrium. The LQR controller shows to have the smallest region of attraction of the compared controllers. The more aggressive controller design of the LQR compared to the SF controller is pointed out by the closed loop eigenvalues, which are closer to the unit circle. The higher aggressiveness of the LQR controller enables it to bring the system faster back to the equilibrium, but it also makes the closed loop system less robust to variations in the initial conditions. The trade-off between these two has to be done when experiments on the vehicle are performed.

At the current stage, the input values are sent to the vehicle via WIFI. Because of the apparent delay caused by this, a controller for the steering input should be implemented on the car to minimize the time delay. A MPC with a long prediction horizon can have high computational demands, which can limit the sampling time when implemented on the hardware on the vehicle.

Considering the performance evaluation experiments and the closed loop phase portraits, a well-designed LQR controller can be sufficient for a good performance for a sustained drift. Where the trade-off between robustness to initial conditions and disturbances has to be evaluated carefully. Furthermore, it should be evaluated experimentally how much the MPC can improve the performance.

6.2 Future work

- It should be evaluated if tyres with a different profile are less prone to dust and dirt in the test environment. To minimize the change in environmental influences between experiments, the floor could be cleaned each time, using a carpet could also decrease the influence of dust and dirt.

- A controller for the longitudinal velocity should be implemented to keep it constant during the ramp steer manoeuvre.

- Further experiments should be performed for the parameter verification. For this it can be helpful to steer the car with the remote control and implement a data logger for this data. The logging of the data sent by the remote will also help to log an input sequence to bring the vehicle close to the equilibrium, where the controller can be activated.

- When the model simulations show a satisfying agreement with the physical vehicle, the different controllers can be redesigned in the way presented in this thesis.

- When a good model of the vehicle exists and an input sequence has been found, a SF controller can be implemented on the vehicle for the sustained drift. With experiments on the vehicle, it can be evaluated which SF gains give good performance in practice, LQR can be used to tune the parameters.

- When a good tuning of parameters has been found, it can be assessed if the MPC formulation in section 4.3 is able to further increase the performance.

- The desired drift equilibria could be varied during the experiments, to achieve drifting with changing slip angles. Especially for this case the MPC should outperform the other controllers, if the following desired drift equilibrium is known for the prediction horizon of the MPC.

- Non-linear MPC could be used to further increase the controller performance.

- Learning based MPC could be used to adjust the parameters of the model during the experiments. This would give a better control performance and make the controller more robust against disturbances.

- Furthermore, the model can be extended to also include the global position as states, this would make it possible to implement position tracking.

7 REFERENCES

[1] J. Sousanis, “Wards Auto,” 08 March 2017. [Online]. Available: http://wardsauto.com/news-analysis/world-vehicle-population-tops-1-billion-units.

[2] N. H. T. S. Association, “transportation.gov,” 2013. [Online]. Available: https://www.transportation.gov/briefing-room/us-department-transportation-releases-policy-automated-vehicle-development.

[3] M. Barth, “Real-World CO2 Impacts of Traffic Congestion,” March, 31, 2008.

[4] J. M. Anderson, Autonomous Vehicle Technology, Santa Monica, California: Rand Corporation, 2006.

[5] WHO, “WHO,” WHO, 01 2017. [Online]. Available: http://www.who.int/mediacentre/factsheets/fs310/en/. [Accessed 22 03 2017].

[6] W. H. Organization, “Global Status Report on Road Safety,” WHO, Geneva, Switzerland, 2009.

[7] NHTSA, “Critical Reasons for Crashes Investigated in the National Motor Vehicle Crash Causation Survey,” NHTSA, New Jersey, USA, 2015.

[8] LongROAD, “Keeping Older Adults Driving Safely: A Research Synthesis of Advanced In-Vehicle Technologies,” AAA foundation for trafic safety, Washington, USA, 2015.

[9] A. Versprille, “National Defense Magazine,” 05 2015. [Online]. Available: http://www.nationaldefensemagazine.org/archive/2015/May/Pages/ResearchersHackIntoDriverlessCarSystemTakeControlofVehicle.aspx.

[10] NHTSA, “NHTSA and Cybersecurity,” NHTSA, Washington, USA, 2016.

[11] K. Hill, “Forbes Magazine,” 19 02 2013. [Online]. Available: https://www.forbes.com/sites/kashmirhill/2013/02/19/the-big-privacy-takeaway-from-tesla-vs-the-new-york-times/#149ef7e42fff.

[12] C. Stupp, “euractiv,” 24 11 2015. [Online]. Available: https://www.euractiv.com/section/digital/news/consumer-groups-expose-manufacturers-for-collecting-data-from-connected-cars/.

[13] E. C. f. transportation, “Preparing a Nation for Autonomous Vehicles,” Eno Center for transportation, Washington, USA, 2013.

[14] A. A. Engineering, “Fact sheet vehicle technology survey,” AAA, Washington, USA, 2016.

[15] A. A. Engineering, “Fact sheet vehicle technology survey - phase II,” AAA, Washington, USA, 2017.

[16] P. Lin, “http://cyberlaw.stanford.edu/,” Stanford University, 30 07 2013. [Online]. Available: http://cyberlaw.stanford.edu/blog/2013/07/ethics-saving-lives-autonomous-cars-are-far-murkier-you-think. [Accessed 22 03 2017].

[17] P. Lin, “The Atlantic,” 08 10 2013. [Online]. Available: https://www.theatlantic.com/technology/archive/2013/10/the-ethics-of-autonomous-cars/280360/.

[18] T. Magazine, “Science: Radio Auto,” 10 August 1925.

[19] N. B. Geddes, Magic Motorways, New York, USA: Random House, 1940.

[20] E. Ackermann, “IEEE Spectrum,” IEEE, 31 08 2016. [Online]. Available: http://spectrum.ieee.org/geek-life/history/selfdriving-cars-were-just-around-the-cornerin-1960. [Accessed 16 03 2017].

[21] C. M. M. K.H.F. Cardew, “The Automatic Steering of Vehicles,” Driver Aids and Abilities Section Road Research Laboratory Crowthorne, Berkshire, UK, 1970.

[22] E. D. Dickmanns, “Vehicles Capable of Dynamic Vision,” Munich, Germany, 1997.

[23] T. Jochem, “No Hands Across America,” 23 07 1995. [Online]. Available: http://www.cs.cmu.edu/~tjochem/nhaa/Journal.html.

[24] K. Iagnemma, “Special Issue on the DARPA Grand Challange,” *Journal of Field Robotics,* pp. 461-660, 2006.

[25] T. Braunschweig, “TU Braunschweig,” 07 10 2010. [Online]. Available: https://magazin.tu-braunschweig.de/pi-post/forschungsfahrzeug-leonie-fahrt-automatisch-auf-dem-braunschweiger-stadtring/.

[26] F. Berlin, “FU Berlin,” 17 09 2011. [Online]. Available: http://www.fu-berlin.de/en/presse/informationen/fup/2011/fup_11_291/.

[27] VisLab, “VisLab,” 12 07 2013. [Online]. Available: http://vislab.it/proud/.

[28] R. Randazzo, “Arizona central,” 27 10 2016. [Online]. Available: http://www.azcentral.com/story/money/business/tech/2016/10/27/google-self-driving-cars-hit-streets-more-phoenix-area-cities/92835208/.

[29] A. Krok, “Cnet,” 01 02 2017. [Online]. Available: https://www.cnet.com/roadshow/news/tesla-is-now-testing-autonomous-vehicles-on-public-california-roads/.

[30] J. Z. e. al, “Kartengestütztes automatisiertes Fahren auf der Bertha-Benz-Route von Mannheim nach Pforzheim,” Karlsruhe, Germany, 2014.

[31] S. Abuelsamid, “Forbes Magazine,” 09 09 2016. [Online]. Available: https://www.forbes.com/sites/samabuelsamid/2016/09/09/volvo-completes-first-autonomous-xc90-for-2017-public-driveme-test-program/#280d5ae91c06.

[32] BMW, “BMW News,” 04 01 2017. [Online]. Available: https://news.bmw.co.uk/article/bmw-self-driving-test-cars-to-be-on-the-roads-in-2017/.

[33] D. Muoio, “Business Insider,” 07 01 2017. [Online]. Available: http://www.businessinsider.com/self-driving-car-milestones-coming-in-2017-2017-1?r=US&IR=T&IR=T/#7-perhaps-the-biggest-milestone-to-prepare-for-in-2017-will-be-when-a-self-driving-tesla-drives-itself-from-los-angeles-to-new-york-7.

[34] K. Kritayakirana, “Autonomous vehicle control at the limits of handling, PHD Thesis,” PHD Thesis at Stanford University, Stanford, USA, 2012.

[35] J. G. K. Kritayakirana, “Autonomous vehicle control at the limits of handling,” International Journal of Vehicle Autonomous Systems, vol. 10 no. 4, 2012.

[36] M. Croft-White, “Measurement and analysis of rally car dynamics at high attitude angles,” PHD. Dissertation Cranfield University, Cranfield, UK, 2006.

[37] R. Y. H. a. J. C. G. C. Voser, “Analysis and control of high sideslip manoeuvres,” Vehicle System Dynamics. vol. 48, pp. 317-336, 2010.

[38] L. K. H. J. C. G. J. C. Kegelman, “Insights into vehicle trajectories at the handling limits: analysing open data from race car drivers,” Vehicle system dynamics, vol. 55 no. 2, p. 191-207, Stanford, USA, 2017.

[39] D. K. E. F. P. T. a. R. H. E. Velenis, “Stabilization of steady-state drifting for a rwd vehicle,” Proceedings of AVEC, 2010.

[40] J. K. a. K. K. H. Nakano, “Control of a Four_Wheel Independently Driven Electric Vehicle with a Large Sideslip Angle,” Robotics and Biometrics, IEEE International Conference Dec. 2014, pp.265-270, 2014.

[41] J. K. a. K. K. Hiroshi Nakano, “Trajectory tracking control of a vehicle with a large sideslip angle,” Advanced Intelligent Mechatronics (AIM), 2015 IEEE International Conference, July 2015, pp. 971-976, 2015.

[42] J. C. G. J. Y. Goh, “Simultaneous Stabilization and Tracking of Basic Automobile Drifting Trajectories,” IEEE Intelligent Vehicle Symposium (IV), June 19-22 2016, 2016.

[43] J. C. G. R. Y. Hindiyeh, “A controller framework for autonomous drifting: Design, stability and experimental validation,” Journal of Dynamic Systems, Measurement and Control vol 136, no. 5, July 2014, 2014.

[44] B. T. C. C. P. M. R. Lenain, “Model Predictive Control for Vehicle Guidance in Presence of Sliding: Application to Farm Vehicles Path Tracking,” IEEE International Conference on Robotics and Automation, April 2005, Barcelona, Spain, 2005.

[45] E. S. M. P. S. M. F. Cheli, “A methodology for vehicle sideslip angle identification: comparison with experimental data,” Vehicle System Dynamics vol. 45, No. 6, June 2007, 2007.

[46] J. C. G. N. R. Kapania, “Design of a feedback-feedforward steering controller for accurate path tracking and stability at the limits of handling,” Vehicle System Dynamics, Vol. 53, No. 12, pp. 1687-1704, 2015.

[47] V. Schlotter, “Einfluss dynamischer Radlastschwankungen und Schräglaufwinkeländerungen auf die horizontale Kraftübertragung von Ackerschlepperreifen,” Universität Stuttgart, Stuttgart, Germany, 2005.

[48] J. Svendenius, “Tire Modeling and Friction Estimation,” Department of Automatic Control Lund University, Lund, Sweden, 2007.

[49] B. W. Jacob Svendenious, “Brush Tire Model With Increased Flexibility,” Department of Automatic Control, Lund Institute of Technology, Lund, Sweden, 2003.

[50] C. B. E. F. Camacho, Model Predictive Control, London, UK: Springer, 2007.

[51] P. O. D. A. L. d. Re, Automotive Model Predictive Control, London, UK: Springer, 2010.

[52] T. f. team, “f1tenth.org,” 2016. [Online]. Available: http://f1tenth.org/misc-docs/BuildInstructions. [Accessed 10 05 2017].

[53] Traxxas, “traxxas.com,” Traxxas, [Online]. Available: https://traxxas.com/products/models/electric/74076rally. [Accessed 10 05 2017].

TRITA EE 2017:089
ISSN 1653-5146